The Thesis Committee for Benjamin Lee Bahorich
Certifies that this is the approved version of the following thesis:

Examining the Effect of Cemented Natural Fractures on Hydraulic Fracture Propagation in Hydrostone Block Experiments

APPROVED BY
SUPERVISING COMMITTEE:

Supervisor:

Jon E. Olson

Jon Holder

Examining the Effect of Cemented Natural Fractures on Hydraulic Fracture Propagation in Hydrostone Block Experiments

by

Benjamin Lee Bahorich, B.S.M.E.

Thesis

Presented to the Faculty of the Graduate School of

The University of Texas at Austin

in Partial Fulfillment

of the Requirements

for the Degree of

Master of Science in Engineering

The University of Texas at Austin

August 2012

Acknowledgements

I thank the Fracture Research and Application Consortium (FRAC) at the University of Texas at Austin for providing funding for this work. I thank Farrukh Hamza, Mehran Hosseini, and Kashif Naseem of The University of Texas at Austin for their help in various parts of the laboratory work. I thank also thank Hanh Nguyen of BJ Services for providing the guar for our fracturing fluid.

Abstract

Examining the Effect of Cemented Natural Fractures on Hydraulic Fracture Propagation in Hydrostone Block Experiments

Benjamin Lee Bahorich, M.S.E.

The University of Texas at Austin, 2012

Supervisor: Jon E. Olson

Micro seismic data and coring studies suggest that hydraulic fractures interact heavily with natural fractures creating complex fracture networks in naturally fractured reservoirs such as the Barnett shale, the Eagle Ford shale, and the Marcellus shale. However, since direct observations of subsurface hydraulic fracture geometries are incomplete or nonexistent, we look to properly scaled experimental research and computer modeling based on realistic assumptions to help us understand fracture intersection geometries. Most experimental analysis of this problem has focused on natural fractures with frictional interfaces. However, core observations from the Barnett and other shale plays suggest that natural fractures are largely cemented. To examine hydraulic fracture interactions with cemented natural fractures, we performed 9 hydraulic fracturing experiments in gypsum cement blocks that contained embedded planar glass, sandstone, and plaster discontinuities which acted as proxies for cemented natural fractures.

There were three main fracture intersection geometries observed in our experimental program. 1) A hydraulic fracture is diverted into a different propagation path(s) along a natural fracture. 2) A taller hydraulic fracture bypasses a shorter natural fracture by propagating around it via height growth while also separating the weakly bonded interface between the natural fracture and the host rock. 3) A hydraulic fracture bypasses a natural fracture and also diverts down it to form separate fractures. The three main factors that seemed to have the strongest influence on fracture intersection geometry were the angle of intersection, the ratio of hydraulic fracture height to natural fracture height, and the differential stress.

Our results show that bypass, separation of weakly bonded interfaces, diversion, and mixed mode propagation are likely in hydraulic fracture intersections with cemented natural fractures. The impact of this finding is that we need fully 3D computer models capable of accounting for bypass and mixed mode I-III fracture propagation in order to realistically simulate subsurface hydraulic fracture geometries.

Table of Contents

List of Tables

List of Figures

Introduction

The Society of Petroleum Engineers estimates that over 1 million fracture stimulation treatments have been conducted in North America (King, 2012). According to a recent study by IHS Global Insight, hydraulic fracturing will allow the average American household to gain $926/year in disposable income between 2012 and 2015 (Mohsen et al., 2011). Clearly, this technology has had an incredible effect on the North American energy industry. However, despite its vast impact, hydraulic fracturing still has much room for optimization because hydraulic fracture / natural fracture interactions are poorly understood.

Complex hydraulic fracture geometry is considered to be a common place occurrence in naturally fractured reservoirs such as tight gas sandstones and shales, largely based on the interpretation of microseismic data (Fisher et al., 2002; Maxwell et al., 2002; Daniels et al., 2007; Le Calvez et al., 2007). The actual resultant geometry from hydraulic fracture treatments in rocks with natural fracture weaknesses, typically pumped from multiple injection zones spaced along extensive horizontal wells, is still a topic of discussion and debate. The best direct evidence of fracture geometry has come from mineback studies, where realistic fracturing fluids have been injected into realistic wellbores, but often at very shallow depths or in igneous or metamorphic rock (Warpinski and Teufel, 1987; Jeffrey et al., 1995). These types of studies report hydraulic fracture diversion along natural planes of weakness such as natural fractures and bedding planes. Multiple fractures can propagate simultaneously parallel to one another, but under many circumstances, one fracture plane will eventually dominate. Coring across hydraulic fracture trends has shown that such multiple parallel fractures are present in tight gas sandstones (Warpinski et al., 1993; Branagan et al., 1996).

Laboratory experiments are another way to investigate the physics of hydraulic fracture complexity, with the advantage of better boundary condition controls and near complete observation of fracture geometry. The drawback of laboratory experiments is potential issues with proper scaling to ensure that results are applicable to actual field operations (de Pater et al., 1994). We performed scaling calculations focusing on recreating the crack propagation physics of crack energy and elastic deformation.

Blanton (1982) studied hydraulic fracture crossing and arrest in frictional interfaces within Devonian shale and hydrostone showing that stress state and approach angle between the hydraulic and natural fracture were key parameters. Renshaw and Pollard (1995) and Gu et al. (2011) expanded on this approach developing crossing criterions based on analytical equations for frictional interfaces. Beugelsdijk et al. (2000) and Zhou and Xue (2011) thermally induced pre-existing fractures in cement blocks to generate a fracture network for the hydraulic fracture to encounter, examining the impact of pre-existing fracture conductivity, stress state and injection rate on fracture path complexity. These experiments showed that natural fracture interaction and reactivation can be detected through treating pressure, and that hydraulic fractures are likely to branch to other connected natural fractures when the differential stress is low. Zhou et al. (2008) represented natural fractures by inserting paper sheets of varying strength into cement blocks to simulate per-existing fractures of various "shear strength". Athavale and Miskimins (2008) examined bonded interfaces between layers to approximate laminated reservoirs. These experimental and analytical approaches all demonstrate that the angle of intersection and the differential stress are key parameters, but none of these approaches take into account the possibility of bypass since the natural fractures span the entire height of the hydraulic fracture.

Our experimental setup is unique compared to other experimental work in three main ways. Firstly, our discontinuities (natural fractures) do not span the entire height of the gypsum cement block allowing hydraulic fractures to grow taller and bypass natural fractures. The field case where hydraulic fractures are taller than the in situ joints they intersect is likely very common in naturally fractured reservoirs because joints are often bounded by bedding planes and are typically a few meters in height or less (Pollard and Aydin, 1988). Hydraulic fractures, on the other hand, are typically around a hundred meters tall (Fisher and Warpinski, 2012). Secondly, our natural fractures are molded into the plaster at the beginning of the curing process creating a natural fracture discontinuity that is bonded to the host rock. This aspect of the experimental setup is motivated by the fact that core observations from the Barnett and other shale plays suggest that natural fractures are largely cemented (Gale et al, 2007). Thirdly, we use different types (glass, Berea sandstone, and gypsum plaster) and sizes of natural fractures so that we can study the effects of varying natural fracture strength, permeability, bond strength, and height.

The objective in this work is to examine the nature of hydraulic fracture interaction with naturally cemented or sealed pre-existing fractures. We inject linear and gel into the block under a true triaxial stress state where the hydraulic fracture path is designed to intersect the embedded inclusions (natural fractures). Our experimental results agree with past work showing that the angle of intersection and the differential stress are key parameters. Furthermore, our experiments show that bypass is likely and that the ratio of hydraulic fracture height (H_{HF}) to natural fracture height (H_{NF}) is another key parameter. Our unique experimental setup allows us to observe complex intersection geometries including combinations of interfacial separation, fracture bypass, diversion, and continued fracture propagation off of natural fracture tip lines. Observing a variety of complex interactions between hydraulic and natural fractures in these experiments can

help us better understand what happens subsurface and give us reason to develop more accurate hydraulic fracturing models.

Experimental Setup

9 tests were carried out on one-foot cubes of gypsum plaster and hydrostone. Samples were poured in three layers with each layer typically being four inches thick. Excluding tests 1a and 1b (see Table 3), the top and bottom layers were hydrostone and the middle layer was gypsum plaster. The top and bottom layers of hydrostone provided a means of vertical containment so that the hydraulic fracture would initiate and propagate within the middle layer only. Tests 1a and 1b were performed with three layers of gypsum plaster (no hydrostone) to examine the effect of uncontained height growth. The hydrostone used was made by United States Gypsum Company (IG-123-F1-50BAG/6-99). The gypsum plaster was made by DAP Products Inc. (55FG-DAP-135094A). Table 1 shows the recipes for hydrostone and plaster by weight.

Material	Dry Cement Weight %	Water Weight %
Hydrostone	75.7	24.3
Gypsum Plaster	63	37

Table 1: Hydrostone Mixing Percentages

Mechanical property tests were carried out on these mixtures by deforming samples poured in core shaped molds. The Mohr-Coulomb shear failure criterion can be written as

$$\sigma_1 = n\sigma_3 + UCS \ , \qquad \text{Eq. 1}$$

where σ_1 is the compressive stress, σ_3 is the confining stress stress, n is the slope of the σ_1 vs. σ_3 plot, and UCS is the unconfined compressive strength (Zoback, 2007, p. 87-92). Figure 1 shows Young's modulus and UCS of gypsum plaster as a function of curing time. The data show that gypsum plaster attains most of its strength and stiffness within

4-5 days. Fully cured gypsum plaster has a Young's modulus of about 200,000 psi and a UCS of about 1,000psi. Figure 2 plots failure stress versus confining stress to quantify the Mohr-Coulomb failure parameters. The slope of the σ_1 vs. σ_3 plot is n=6.33. Using the relation

$$\mu_i = \frac{n-1}{2\sqrt{n}} \qquad \text{Eq. 2}$$

results in a internal friction coefficient of μ_i =1.06. The y-intercept is 1080 psi which agrees well with the directly measured UCS values. Using the relation

$$S_0 = \frac{UCS}{2\left(\sqrt{\mu_i^2+1}+\mu_i\right)} \qquad \text{Eq. 3}$$

the internal cohesion (S_0) of gypsum plaster is calculated to be 214.5psi (Zoback, 2007, p. 87-92). Figure 3 shows Young's modulus and UCS of hydrostone as a function of curing time. A comparison of figure 1 and figure 3 shows that, although Young's modulus may be similar between gypsum plaster and hydrostone, the compressive strength of hydrostone is much higher than that of gypsum plaster. We performed Brazilian tests (ASTM D3967-08) to determine tensile strength and semicircular bending tests to determine mode I fracture toughness (Chong and Kuruppu, 1984). The tensile strength of hydrostone and gypsum plaster was measured to be 700 psi and 294 psi respectively (Table 2). The fracture toughness of hydrostone and gypsum plaster was measured to be 0.28 $MPa\sqrt{m}$ and 0.12 $MPa\sqrt{m}$ respectively (Table 4). All of our hydraulic fracturing experiments with hydrostone layers on top and bottom maintained containment of the hydraulic fracture within the middle layer of gypsum plaster. This containment was probably due to the fracture toughness of hydrostone being higher than the fracture toughness of gypsum plaster. We also performed permeability tests on fully cured hydrostone and fully cured gypsum plaster using a nitrogen gas permeameter. The

permeability of hydrostone and gypsum plaster was measured to be 7.2 mD and 57.3 mD respectively (Table 2).

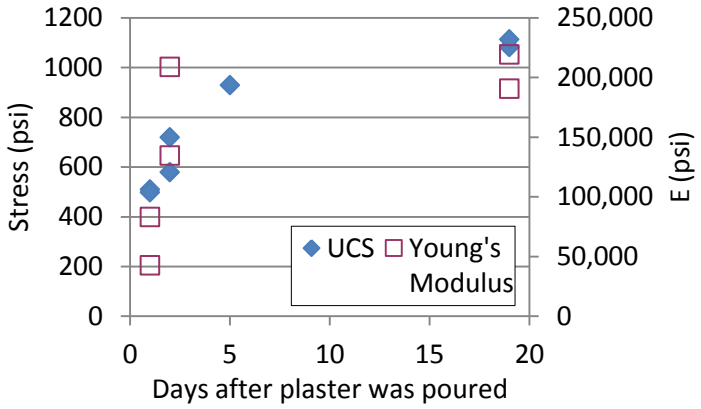

Figure 1. Unconfined compressive strength and Young's modulus vs. curing time for gypsum plaster.

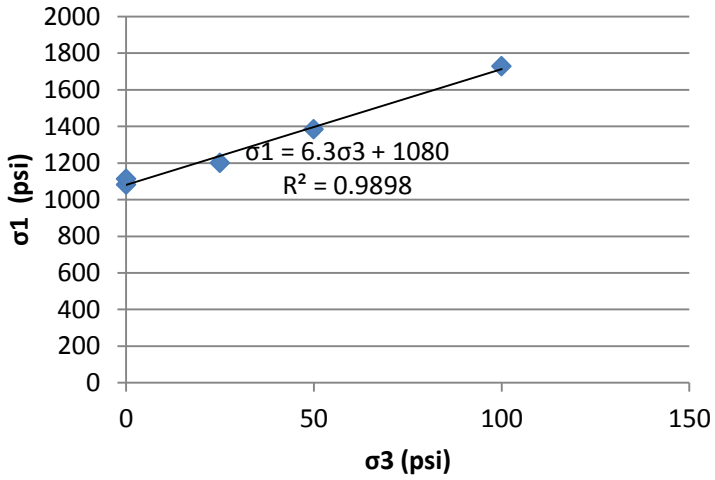

Figure 2. Maximum compressive strength of gypsum plaster vs. confining pressure.

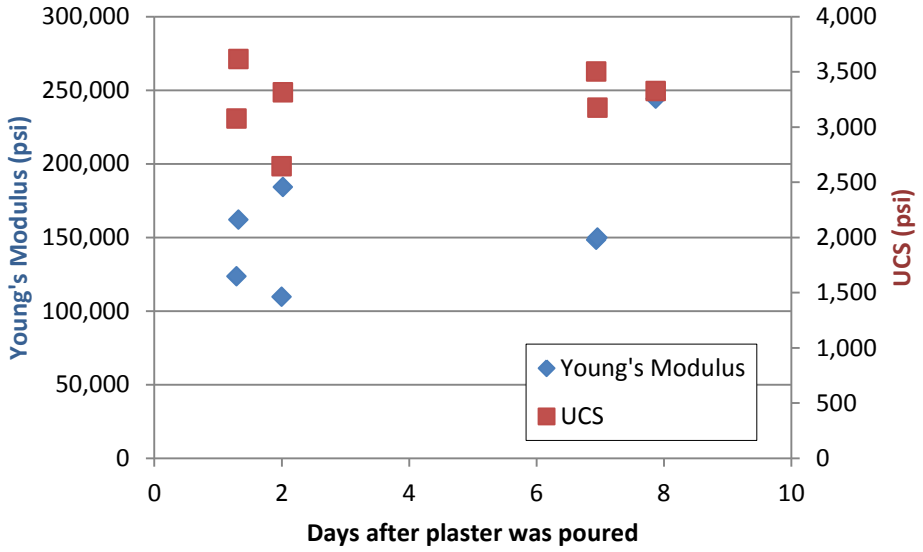

Figure 3. Unconfined compressive strength and Young's modulus vs. curing time for hydrostone.

Material	Tensile Strength (psi)	Permeability (mD)
Hydrostone	700	7.2
Gypsum Plaster	294	57.3

Table 2: Mode I Fracture Toughness, Tensile Strength, and Permeability of Hydrostone and Gypsum Plaster

The wellbore was made from 3/8th inch (outer diameter) copper or aluminum tubing placed in the central area of the block prior to pouring (Figure 4 and Figure 5). To mimic an open hole completion, a nylon tube was inserted through the copper tubing to stick out the end of the wellbore by about 1 inch. To represent perforations, the embedded end of the wellbore was plugged, and nylon strings were threaded out holes drilled in the side of the wellbore. After the block hardened, the nylon strings or tubes were pulled out of the wellbore to leave space for the fluid to initiate a fracture. Natural

fractures were modeled with thin slides of glass, thin slides of Berea sandstone and thin slides of cured gypsum plaster. These thin slides (natural fractures) were placed near the wellbore either orthogonal or oblique to the direction of S_{Hmax} to ensure hydraulic fracture / natural fracture intersection. We used two main sizes of natural fractures with one size being taller than the other size (Figure 6). The taller slides (natural fractures) measured 1.55 in. tall by 3 in. long by 0.1 in. thick. The shorter slides (natural fractures) measured 1 in. tall by 3 in. long by 0.1 in thick. We utilized different sizes of natural fractures in order to observe the effects of relative fracture size on hydraulic fracture / natural fracture intersection geometry. The natural fractures were made of Berea sandstone, glass, and gypsum plaster.

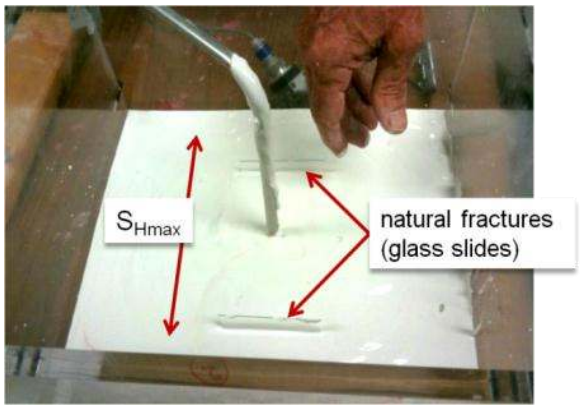

Figure 4. A test block in preparation with two glass slides set in the middle layer of plaster as it is being poured.

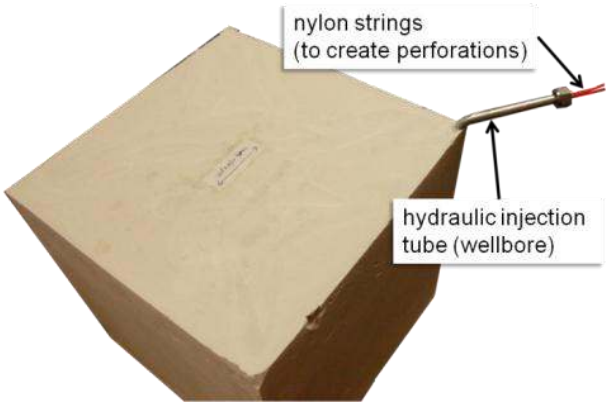

Figure 5. A finished block sample that is ready to be hydraulically fractured. The ends of the nylon perforation strings are threaded out both ends of the wellbore before pouring the plaster. After the block is cured, the strings are pulled out leaving perforations in place.

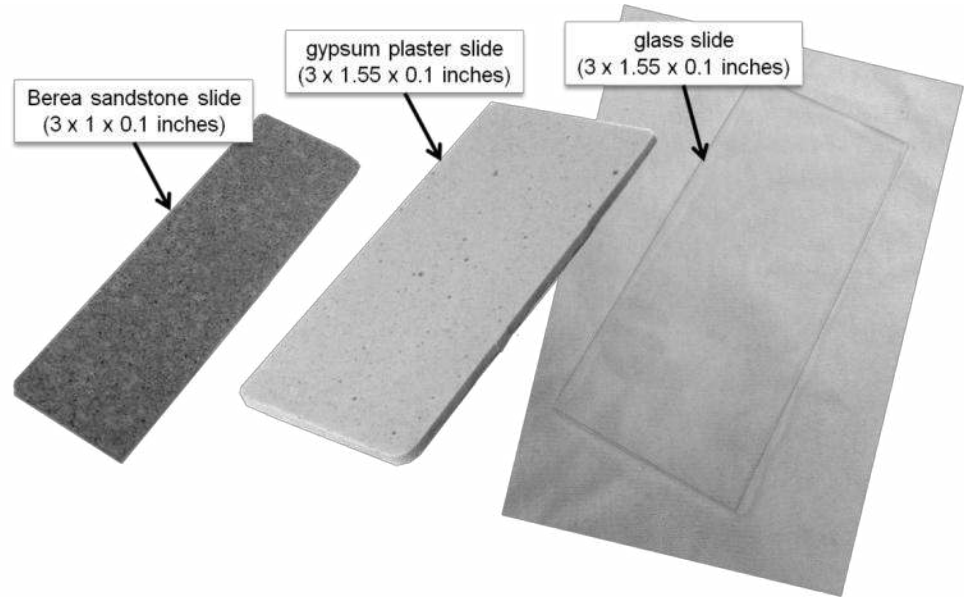

Figure 6. The three types of natural fractures embedded in the blocks. The gypsum plaster slides and the glass slides had the same dimensions and were taller than Berea sandstone slides.

After pouring the plaster, the block would become relatively hard after about one hour. At this point, the block was taken out of the acrylic form and was allowed to cure for several days. After waiting for the block to reach full strength (about 10 days of

curing), the block was placed in the aluminum walled apparatus for testing. Figure 7 (left) shows the inside of the aluminum box with the two rubber flat jacks used to apply horizontal stresses. A third flat jack was placed between the top of the block and the apparatus lid to apply the vertical stress. In Figure 7 (right) the box is closed and the flat jacks are connected to their air supply (each flat jack is rated at 100 psi maximum). Tests were run with S_1=100psi (S_v), S_2=75psi (S_{Hmax}) and 25psi≤S_3≤60psi (S_{Hmin}).

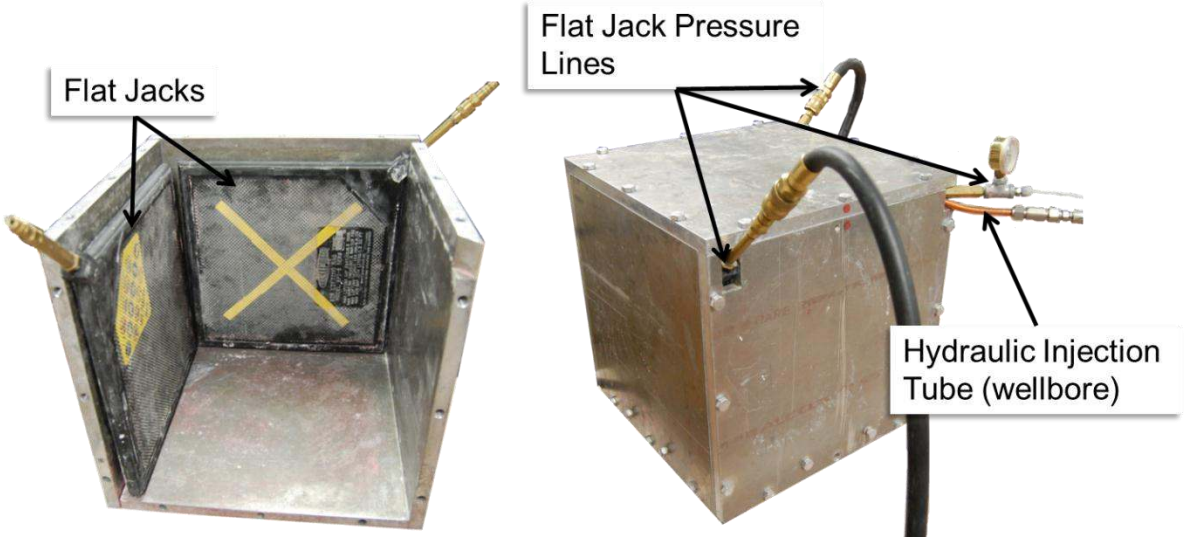

Figure 7. The aluminum box used for containment of hydraulic fracture specimens. Left shows the partially dismantled aluminum box with flat jacks. Right displays the sealed box with flat jacks connected to independent air supplies.

A Teledyne ISCO 1000D syringe pump with a one liter capacity was used to inject the fracturing fluid. Fluid pressures were monitored by transducers at the pump chamber and at the entrance to the wellbore. In the event that more than one liter of fluid was needed, injection was halted, the accumulator was refilled, and the pumping was resumed. The fracturing fluid used was a linear guar-based gel (GW-38 acquired from BJ Services) mixed at 42 lbs gel powder per 1000 gallons water. We added a red dye so that we could easily see the hydraulic fracture path when we broke open the block. Using

a viscometer, the apparent viscosity (μ) of the fracturing fluid was measured to be 118 cp at a shear rate of 39.3 1/s. Using the equation

$$\mu = k \left|\frac{du}{dy}\right|^{n-1}, \qquad \text{Eq. 4}$$

the value for k was measured to be 170.6 and n was measured to be 0.9 Most of our hydraulic fracturing tests were performed at a flow rate of about 200 ml/min.

We ran three tests with each type of slide (glass, plaster, and Berea sandstone). The tests were run with varying configurations of natural fractures, but most tests contained some slides that were orthogonal to the direction of S_{Hmax}, and some slides that were oblique to the direction of S_{Hmax} (see Figure 4 for a sample configuration). Table 3 contains a list of tests and experimental setups. All tests except 1b contained a main hydraulic fracture which propagated perpendicular to S_3 (S_{Hmin}). Test 1b was unique in that the main hydraulic fracture initiated and propagated through the sample in a horizontal direction such that fracture propagation was roughly perpendicular to the maximum principal stress (S_v). It is unclear why this was the case, but it could have something to do with the orientation of the perforations that were slightly deviated from their intended vertical direction.

Test	Natural Fracture Type	Wellbore Orientation	Orientation of Perforations	Natural Fracture Height	S_V (psi)	S_{Hmax} (psi)	S_{Hmin} (psi)	Horizontal Differential Stress (psi)
1a	glass	horizontal	vertical	tall	100	75	25	50
1b	glass	horizontal	slightly off from vertical	tall	100	75	25	50
1c	glass	vertical	parallel to S_{Hmax}	tall	100	75	25	50
2a	Berea sandstone	vertical	parallel to S_{Hmax}	short	100	75	25	50
2b	Berea sandstone	vertical	parallel to S_{Hmax}	short	100	75	45	30
2c	Berea sandstone	vertical	parallel to S_{Hmax}	short	100	75	60	15
3a	gypsum plaster	vertical	parallel to S_{Hmax}	tall	100	75	25	50
3b	gypsum plaster	vertical	parallel to S_{Hmax}	tall	100	75	45	30
3c	gypsum plaster	vertical	parallel to S_{Hmax}	tall	100	75	60	15

Table 3: Test Samples with Experimental Setup

After fracturing a sample, the block was broken open with a hammer and chisel (Figure 8). For more planar fractures, the block easily split open along the fracture with little effort by hammering along the plane of the fracture. However, in the case of more complex fractures, more detailed sculpting was required to uncover the fracture.

Figure 8. The dismantling of a specimen by chiseling after hydraulic fracturing.

SEMICIRCULAR BENDING TESTS

We performed semicircular bending tests (Chong and Kuruppu, 1984) on gypsum plaster, hydrostone, and sandstone in order to determine the fracture toughness (K_{IC}) of these different materials. K_{IC} is calculated as a function of peak load using

$$K_I = \frac{P\sqrt{\pi a}}{DB} Y_I \ , \qquad \text{Eq. 5}$$

where P is the maximum load, a is the crack length, D is the diameter, B is the thickness, and Y_I is the dimensionless coefficient. We used the equation

$$Y_I = 4.782 - 1.219\frac{a}{r} + 0.063 \exp\left(7.045\left(\frac{a}{r}\right)\right) \ , \qquad \text{Eq. 6}$$

for Y_I developed by Lim et al. (1994) who demonstrated its applicability for soft rock.

The constraints on the values of a and r are that $0.03 \leq a/r \leq 0.5$ and that $s/r = 0.8$ (see Figure 9 for a labeled depiction of the SCB test). The data for these different tests can be found in Table 4. The average K_{IC} of hydrostone and Berea sandstone was determined to be 0.28 MPa$\sqrt{m}$), and the average K_{IC} of gypsum plaster was determined to be 0.12 MPa$\sqrt{m}$.

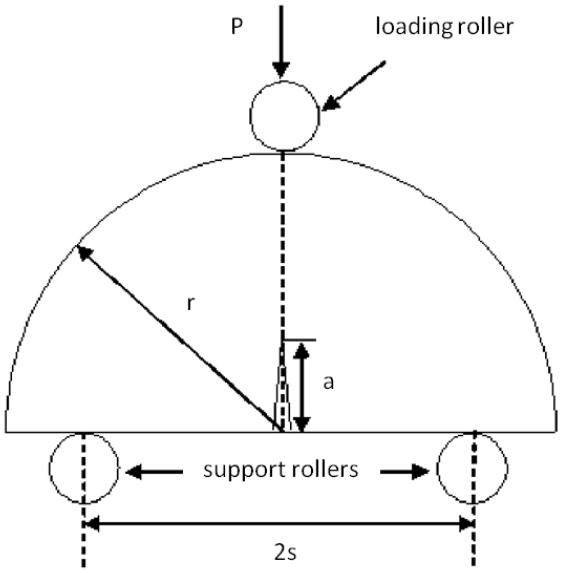

Figure 9. A labeled depiction of the SCB test.

Sample	B (in)	a (in)	D (in)	Max Load (lbs)	K_{Ic} (MPa * m^.5)	Average K_{Ic} (MPa * m^.5)
Hydrostone 1	0.56	0.24	1.45	45.11	0.27	
Hydrostone 2	0.55	0.24	1.45	47.54	0.29	Hydrostone
Hydrostone 3	0.52	0.24	1.45	44.29	0.28	0.28
Plaster 1	0.44	0.24	1.45	14.62	0.11	
Plaster 2	0.49	0.24	1.45	19.90	0.13	
Plaster 3	0.41	0.24	1.45	15.02	0.12	Plaster
Plaster 4	0.42	0.24	1.45	16.73	0.13	0.12
Berea Sandstone 1	0.48	0.28	2.04	54.65	0.28	
Berea Sandstone 2	0.46	0.28	2.04	54.65	0.29	Berea
Berea Sandstone 3	0.48	0.28	2.04	54.65	0.28	0.28

Table 4: SCB Tests on Hydrostone, Gypsum Plaster, and Berea Sandstone

Cement bond strength is one of the parameters that could have a strong effect on fracture intersection geometry. In order to determine the cement bond strength of the different types of natural fractures that we used in our hydraulic fracturing experiments

we performed modified SCB tests with “natural fracture” inclusions. Our semi-circular bending test samples were made of gypsum plaster host rock surrounding planar inclusions of glass, Berea sandstone, and gypsum plaster. We embedded these discontinuities such that the planar interface between the discontinuity and the gypsum plaster host rock was right in the middle of the semicircular sample extending from the notch as shown in Figure 10.

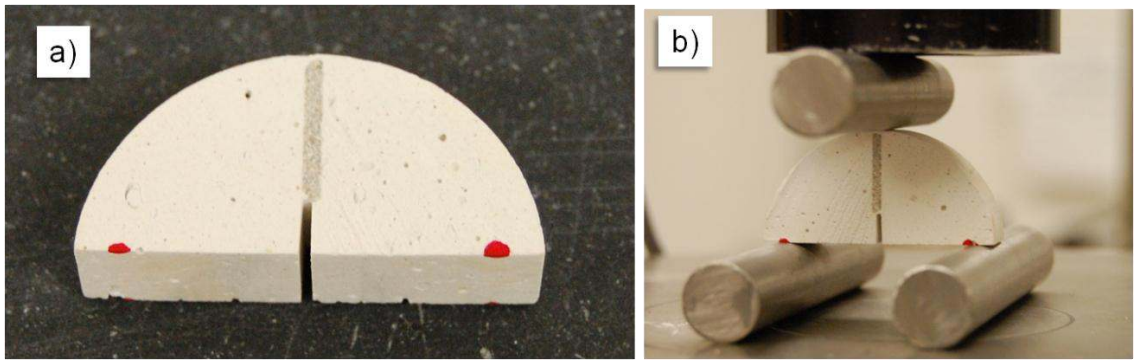

Figure 10. Semicircular bend tests. Part a) depicts a plaster semicircular bending test sample with a Berea sandstone planar discontinuity. Part b) depicts a sample ready to be tested on the compressive load frame.

Figure 10 depicts a semicircular bending test sample with a sandstone discontinuity, but we also performed tests on samples with glass and plaster discontinuities as shown in Figure 11. We created the SCB samples by pouring gypsum plaster into 0.5 inch high semicircular molds. The bottom of the mold was sealed with tape so that the planar discontinuity would stay in place when we placed it before pouring the plaster. The different discontinuities were cut to the appropriate shape beforehand and the rough edges of the cured samples were ground down to ensure sample uniformity.

Figure 11. Gypsum plaster SCB specimens after testing. The samples on the left contain Berea sandstone discontinuities. The samples in the middle contain gypsum plaster discontinuities. And, the samples on the right contain glass discontinuities.

Considering that the SCB test equation (Eq. 5) assumes that the sample is homogeneous, we realize that these tests don't give us completely accurate results for the fracture toughness of the Berea-plaster bond and glass-plaster bond. However, in the case of the plaster-plaster samples (the middle column of specimens in Figure 11), the SCB test should give us an accurate result for the fracture toughness of the bond because the inclusion is the same material as the host rock.

The plaster-plaster bond was measured to have a fracture toughness of about 0.1 MPa$\sqrt{m}$. This is not too far off from the value of the plaster fracture toughness of 0.12 MPa$\sqrt{m}$) which means that the plaster-plaster bond is relatively strong. The fracture toughness for the Berea-plaster bond was measured at 0.09 MPa$\sqrt{m}$ which is close to the value for the plaster-plaster bond. Despite the differing materials, we can conclude that the Berea-plaster bond is stronger than glass-plaster because the glass-plaster bond measured a fracture toughness of only 0.06 MPa$\sqrt{m}$. In fact, it was very difficult to

prepare SCB samples with glass inclusions because they were likely to fall apart due to the weakness of the bond. Given this information, it is safe to assume that the glass-plaster bond is very low strength compared to the plaster-plaster bond and the Berea-plaster bond. Table 5 shows the results for the SCB tests with "natural fracture" inclusions.

Inclusion Type and Sample #	B (in)	a (in)	D (in)	Max Load (lbs)	K_{Ic} (MPa * m^.5)	Average K_{Ic} (MPa * m^.5)
Berea Sandstone 1	0.47	0.19	1.60	15.14	0.08	
Berea Sandstone 2	0.45	0.19	1.60	16.79	0.10	Berea
Berea Sandstone 3	0.40	0.20	1.60	13.50	0.09	0.09
Glass 1	0.40	0.23	1.60	15.14	0.11	
Glass 2	0.40	0.25	1.60	5.27	0.04	Glass
Glass 3	0.40	0.25	1.60	5.21	0.04	0.06
Plaster 1	0.36	0.23	1.58	6.03	0.05	
Plaster 2	0.35	0.23	1.58	14.26	0.12	Plaster
Plaster 3	0.36	0.23	1.58	15.90	0.13	0.10

Table 5: SCB Tests on Gypsum Plaster Samples with Inclusions

As shown in Figure 11, the samples broke down the middle of the specimens. The samples with the plaster discontinuities and the samples with the glass discontinuities showed complete interfacial separation as the cracks propagated along the interface between the discontinuity (natural fracture) and the host rock. However, the samples with the Berea discontinuities cracked mostly through the middle of the Berea discontinuity (there also existed some visible interfacial separation on the face of these cracks). This result seems to indicate that the sandstone is not as tough as the bond between the Berea and the plaster host rock. However, since the fracture toughness of Berea is higher than the fracture toughness of plaster (0.28 MPa$\sqrt{m}$ vs. 0.12 MPa$\sqrt{m}$), it is more likely that this splitting of the sandstone was due to the mechanical differences between plaster and

sandstone as the SCB test assumes that the sample has homogeneous mechanical properties. Berea sandstone has a higher Young's modulus than gypsum plaster does, so it is likely that the Berea sandstone is at a higher stress than the gypsum plaster is at crack initiation.

SCALING CALCULATIONS

Scaling is an important aspect to investigate for all experimental work. Correct scaling means that the physics of fluid driven fracture propagation at the scale of field operations are represented at the scale of lab experiments. If lab experiments do not scale well to field operations, the conclusions might not be very applicable. De Pater et al. (1994a) developed a set of dimensionless groups that can adequately describe the physics of fracture propagation. These dimensionless groups allow us to compare our lab experiments with field operations to make sure our experimental results can be applied at the field scale. Following the method of De Pater et al. (1994b), the dimensionless groups that we analyzed were time, crack energy, elastic deformation, leakoff, and confining stress.

We analyzed how our lab tests scale with two different types of field tests (a slick water fracturing treatment, and a cross-linked gel fracturing treatment). Table 6 shows the input variables used to calculate the dimensionless groups, and Table 8 shows the values of the dimensionless groups, each for laboratory and field conditions. Table 7 shows the input variables for our lab experiments to calculate the leakoff coefficient using the method described in SPE Monograph Volume 12, Chapter 8. Table 8 also shows the ratios of the lab to field values of each dimensionless group. For a specific dimensionless group, a lab to field ratio equal to one would mean that the fracture propagation physics in our lab experiments accurately represents the fracture propagation physics in a typical

field fracture treatment for that specific aspect of fracture propagation. The further the ratio is from one, the more poorly scaled the experiment is for that parameter.

Variable	Units	Lab	Field (slick water)	Field (gel)
time (t)	hours	0.11	1	1
slurry rate (i)	bbls/min	0.0011	50	20
wellbore radius (r_w)	inches	0.1875	2.5	2.5
mode I toughness (K_{Ic})	$MPa\sqrt{m}$	0.12	1.29	1.29
Poisson's ratio (v)	[/]	0.32	0.32	0.32
Young's modulus (E)	psi	150,000	6,000,000	6,000,000
$\bar{E}$	psi	41,778	1,671,123	1,671,123
viscosity (μ)	cp	118	10	500
$\bar{\mu}$	cp	1,416	120	6,000
confining pressure (σ_c)	psi	75	5,000	5,000

Table 6: Dimensionless Group Variables

Variable	Units	Lab
fluid viscosity (μ)	cp	110
filtrate perm (k_f)	Darcy	0.0573
leakoff pressure (ΔP)	psi	200
porosity (φ)	[/]	0.51
fracture surface area (A)	cm^2	232.43
slope (m)	cm^3/(min^.5)	65.00
fluid compressibility (c_t)	1/psi	3.52E-06
reservoir perm (k_r)	Darcy	0.0573
reservoir fluid viscosity (μ_r)	cp	0.0183
C_v	$ft/\sqrt{min}$	0.0025
C_c	$ft/\sqrt{min}$	0.018
C_w	$ft/\sqrt{min}$	0.0046
C_t	$ft/\sqrt{min}$	0.0021

Table 7: Leakoff Coefficients and Determining Variables

Dimensionless Group	Equation	Lab	Field (slick water)	Lab / Field (slick water)	field (gel)	lab/field (gel)
time	$N_t = \frac{ti}{r_w^3}$	0.019	3.2	0.0050	1.28	0.0124
crack energy	$K_\Gamma = \frac{{K_{Ic}}^2}{4\bar{E}^2 r_w}$	1.13E-11	5.96E-14	190.3	5.96E-14	190.3
elastic deformation	$N_{\bar{E}} = \frac{\bar{E} r_w^3}{i\bar{\mu}}$	171.8	4351.9	0.039	217.59	0.79
leakoff	$K_l \sqrt{\frac{r_w}{i}}$	0.0265	0.0010	25.8	0.00014	187.32
confining stress	$N_{\sigma c} = \frac{\sigma_c}{\bar{E}}$	0.0018	0.0030	0.4	0.002992	0.4

Table 8: Dimensionless Groups

The field values in Table 6 are based off of a typical fracture treatment stage in a shale resource play such as the Barnett. We assume 5 inch casing, a confining stress of 5,000 psi, a Young's modulus of 6,000,000 psi, and a Poisson's ratio of 0.32. The slick water treatment scenario assumes a low viscosity fluid (10 cp) and a fast slurry rate (100 bbls/min). 50 bbls/min is shown because we assume that there are two perforation clusters per stage and that our single perforation in our experiment scales to one perforation cluster in the field. The gel treatment scenario assumes a high viscosity fluid (500 cp) and a slower slurry rate (40 bbls/min). Again, we assume two perforation clusters per stage, so 20 bbls/min is shown. The field leakoff coefficient for the slick water scenario was assumed to be 0.0046 $ft/\sqrt{min}$ which is a model-estimated leakoff coefficient for a slick water type fracturing treatment in the Barnett (Grieser et al., 2003). The leakoff coefficient for the gel scenario was assumed to be much lower at 0.0004 $ft/\sqrt{min}$ due to the higher viscosity fracturing fluid.

Due to operational limitations, none of our lab to field ratios are exactly equal to one; however the lab to field ratio for the dimensionless group of confining stress, ($N_{\sigma c}$), is 0.4 which is pretty close to one for both slick water and gel stimulation scenarios. This means that confining stress should have a similar effect on our lab experiments as it does

in the field. Differential stress has a large influence on fracture intersection geometry (Blanton, 1982), so it is important that this ratio be close to one.

For the time dimensionless group and the elastic deformation dimensionless group, our lab experiments more closely scale to the cross-linked gel fracture treatment scenario. In fact, the lab to field ratio for the elastic deformation dimensionless group in the gel scenario is 0.79 which is very close to 1. The elastic deformation dimensionless group takes into account the viscous forces of the fracturing fluid, so our lab experiments should be similar in regards to the viscous forces when compared to a field fracture stimulation with a high viscosity gel.

The crack energy dimensionless group contains the effect of fracture toughness, and the lab to field ratio for both the slick water scenario and gel scenario is 190. This indicates that the fracture toughness should have a larger effect on fracture intersection geometry in our experiments than it might have in a typical field fracture treatment.

For the leakoff dimensionless group, our lab experiments more closely scale to the slick water scenario; however, neither lab to field ratio is very close to one (lab to field ratio of 25.8 for slick water and 187.3 for gel). The permeability of our gypsum plaster is too high compared to the permeability of a tight shale such as the Barnett which prevents the leakoff coefficient from being very close. If we would have used a higher viscosity gel in our experiments, the leakoff coefficient would have been able to be close to one, but that would have influenced our lab to field ratio for elastic deformation negatively.

Results and Discussion

Our investigation of hydraulic fracture / natural fracture interaction was limited to the case of cemented natural fractures only. As mentioned above, the cemented natural fractures were plaster (same strength as the host material), glass and sandstone (both stronger than the host block). There were three main interaction geometries observed: 1) A hydraulic fracture is diverted into a different propagation path(s) by a natural fracture. In this case, a diverted fracture begins an entirely new fracture path after kinking off the end of a natural fracture to continue propagating further. 2) A taller hydraulic bypasses a shorter natural fracture by propagating around it via height growth while also separating the weakly bonded interface between the natural fracture and the host rock. This usually happened for orthogonal approach angles, and it was more likely to occur when the hydraulic fracture was much taller than the natural fracture. 3) A hydraulic fracture bypasses a natural fracture and diverts down it to form separate fractures. In some cases, the hydraulic fracture split into two or three completely separate paths that did not coalesce. In other cases, the diverted fracture(s) would coalesce with a more prominent fracture shortly after diversion. This generally happened when the natural fracture caused the hydraulic fracture(s) to divert only slightly from the original path.

DIVERSION ALONG A NATURAL FRACTURE

The diversion of hydraulic fracture propagation starts with separation of host-rock / natural fracture bond (Figure 12). The angle of intersection (θ) is measured counter-clockwise positive from the initial propagation direction of the hydraulic fracture (Figure 13). The interfacial failure allows fracture fluid to permeate along the natural fracture and pressurize it. Although the figure depicts the weakly bonded plane opening up only to

one side of the hydraulic fracture, in most of our experiments the interface was opened in both directions.

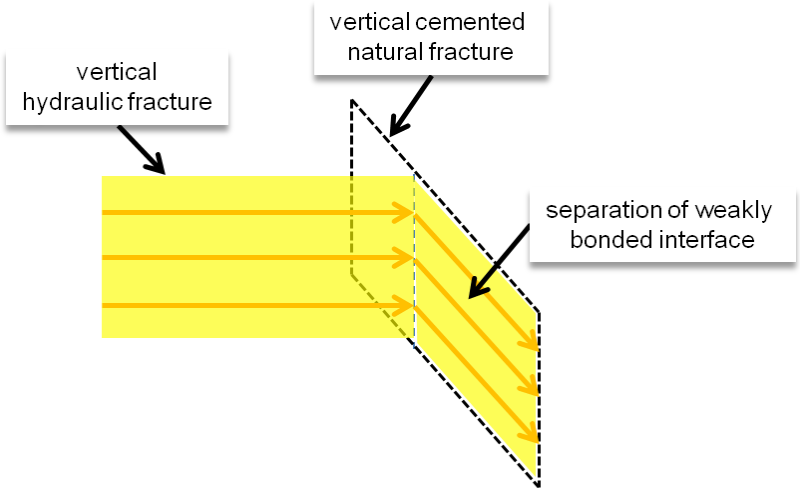

Figure 12. A depiction of the separation of a weakly bonded interface between a cemented natural fracture and the host rock due to the intersection of a hydraulic fracture. The hydraulic fluid is highlighted in yellow and the arrows are the propagation directions.

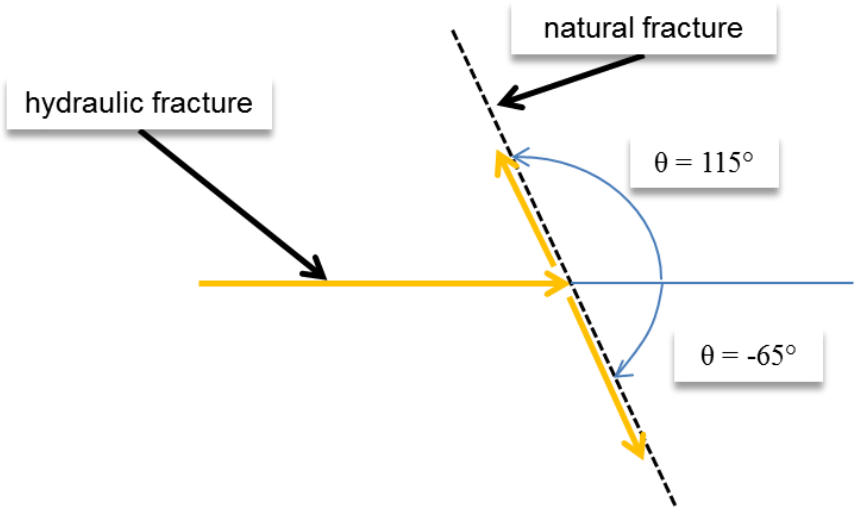

Figure 13. A map view of a vertical hydraulic fracture intersecting and diverting along a vertical natural fracture. The yellow arrows are the propagation directions of the hydraulic fracture, and the dashed line is the vertical natural fracture. The angle of intersection (θ) is measured from the initial propagation direction of the hydraulic fracture (counter-clockwise is positive).

In some cases, after the interfacial failure and separation, the fluid pressure was sufficient to continue fracture propagation by extending from the natural fracture tiplines (Figure 14). This diversion of hydraulic fracture propagation to the natural fracture was observed in Test 3c (Figure 15) and tests 3a, 3b, and 1c. Fluid driven fracture propagation is indicated by the faces that are colored pink (from the dye used in the fracturing fluid). The yellow arrows represent the interpreted fracture propagation path. The fracture initially starts to propagate from the perforations in the S_{Hmax} direction as expected. As the fracture approaches oblique natural fracture outlined with the black rectangle (the dashed portion is to indicate where the natural fracture is hidden), it curves to the right to asymptotically intersect the natural fracture (θ = -70°). This curving was probably made possible by the lower horizontal differential stress (15psi) in this case (S_{Hmax} = 75psi, and S_{Hmin} = 60psi). In other experiments with higher differential stress, the intersection approach was more planar. After the fracture propagated beyond the first natural fracture,

it encountered another natural fracture and followed a similar diverting path. The pump record for this test is shown in Figure 16.

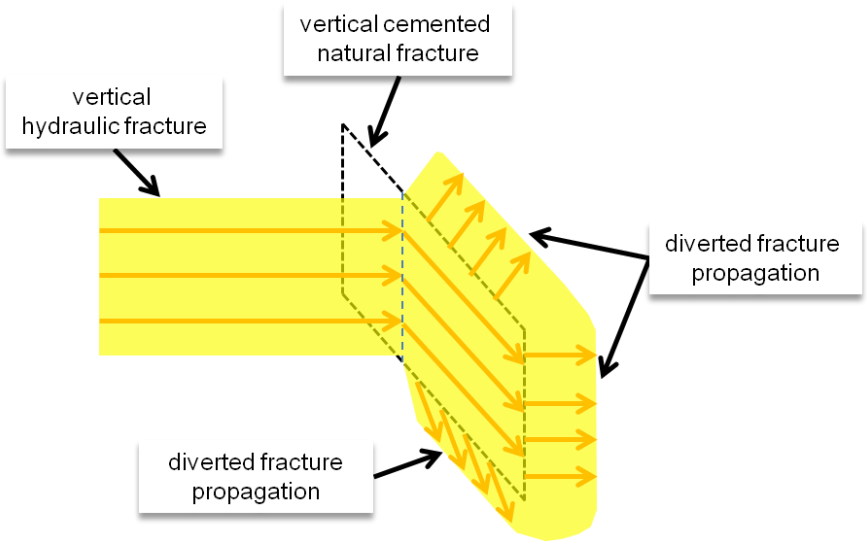

Figure 14. A depiction of hydraulic fracture diversion. Diversion is labeled as "diverted fracture propagation". The hydraulic fluid is highlighted in yellow and the arrows are the propagation directions.

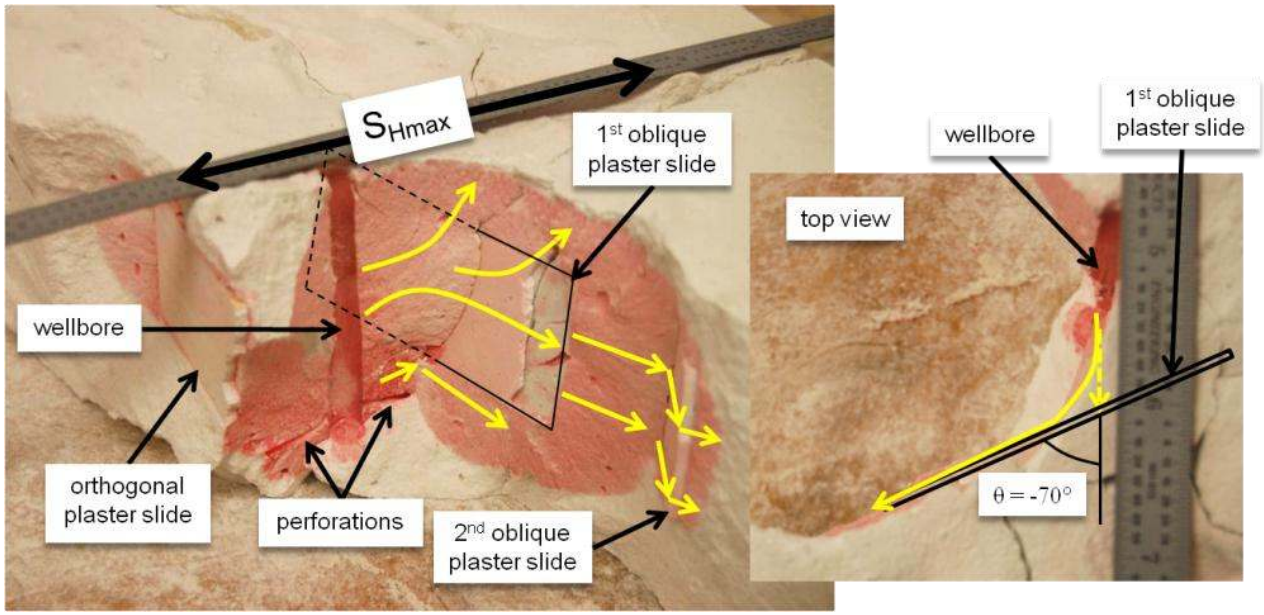

Figure 15. Test 3c exhibiting diversion of a vertical fracture away from the direction of S_{Hmax}. The hydraulic fracture is shown by the faces that are colored pink. The yellow arrows indicated the interpreted path of propagation. The pink coloring is due to the red dye that we mixed into the fracturing fluid. The 1st oblique natural fracture is outlined by the rectangle (the dashed part of the rectangle indicates the part of the natural fracture behind the face of the hydraulic fracture). The inset shows a top view so that the angle of intersection can easily be seen. The wellbore is vertical.

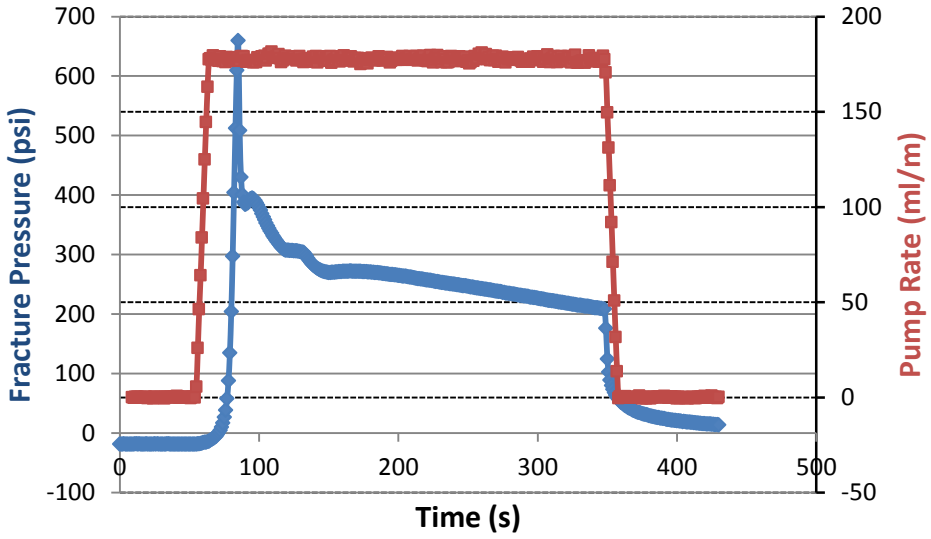

Figure 16. The pump pressure record for the fracture in Figure 15 (Test 3c).

NATURAL FRACTURE BYPASS

The second type of fracture interaction observed in our experiments was interfacial separation coupled with vertical bypass around a natural fracture (Figure 17). The approaching hydraulic fracture does not break through the natural fracture but propagates around it, which allows it to maintain a constant, planar orientation. There is still interfacial separation and fluid intrusion along the natural fracture, but no additional propagation beyond the original natural fracture tips.

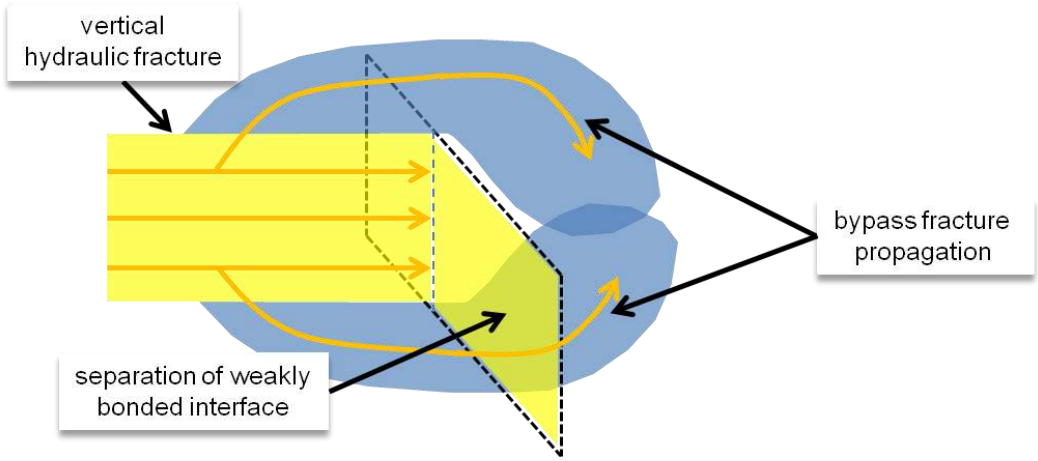

Figure 17. A depiction of hydraulic fracture vertical bypass. The bypass portion of the hydraulic fracture propagation is colored blue and the initial hydraulic fracture and the separation of the weakly bonded interface is shown in yellow. Arrows indicate propagation direction.

Test 1a (Figure 18) is an example of propagation bypass with an orthogonal glass slide as the natural fracture. Since the hydraulic fracture was taller (or at least was free to grow taller), it propagated around the glass slide (a bypass) instead of being diverted down the glass slide (into the page). The photo is taken looking in the direction of the wellbore which was placed parallel to S_3. The yellow arrows represent the interpreted fracture propagation path based off of the small but noticeable plumose structure on the face of the fracture. The hydraulic fracture initiated from the two perforations in a plane orthogonal to S_3 in a manner analogous to a transverse fracture from a horizontal well. In the process of bypassing the glass slide, the fluid-driven fracture propagates up the back side (away from the wellbore) of the glass slide, which could give the impression that the hydraulic fracture actually crossed the glass slide when it did not.

The greater strength of the glass slides compared to the gypsum plaster was intentional to mimic strongly cemented natural fractures (quartz cement in a weak shale), but another feature that may or may not be analogous to such cemented fractures is the

fact that the glass is impermeable, so the fluid cannot pass through without breaking the slide. It is probably true that completely cemented and sealed natural fractures are less permeable than the host rock around them, but in many situations there is only partial mineralization (Laubach, 2003), where it is likely that permeability in the cross-fracture direction still exists. The effect of natural fracture permeability is an aspect we explored by using thin slides of sandstone and thin slides of plaster as natural fractures (see Table 2 for permeability values).

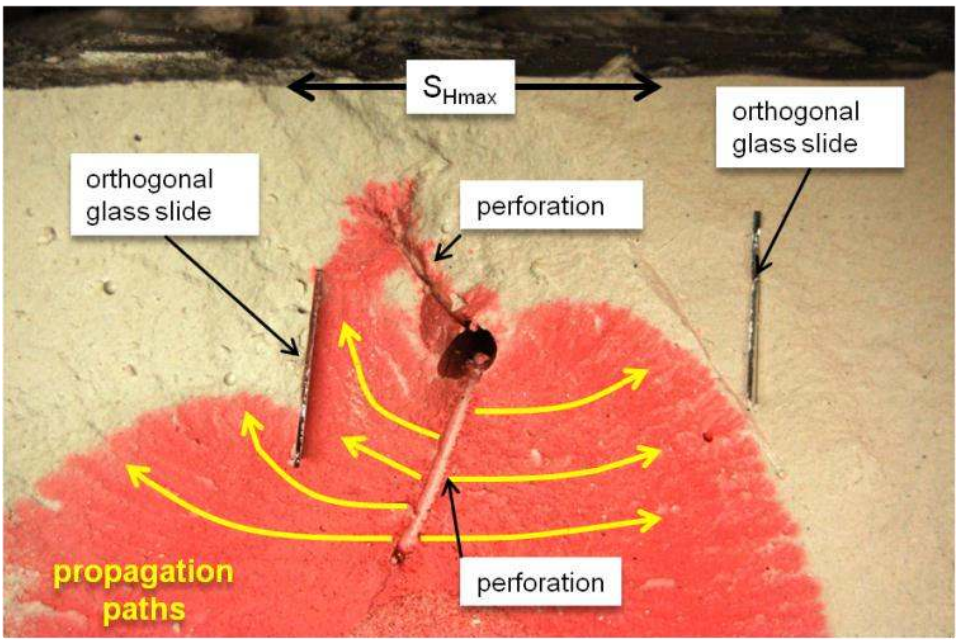

Figure 18. Test 1a exhibiting a hydraulic fracture in the plane of the photo (dyed red) propagating from perforations in that same plane. The wellbore is oriented perpendicular to the plane of the photo as are the glass slides (natural fractures). Yellow arrows represent interpretation of the propagation path of the fracture from the perforation.

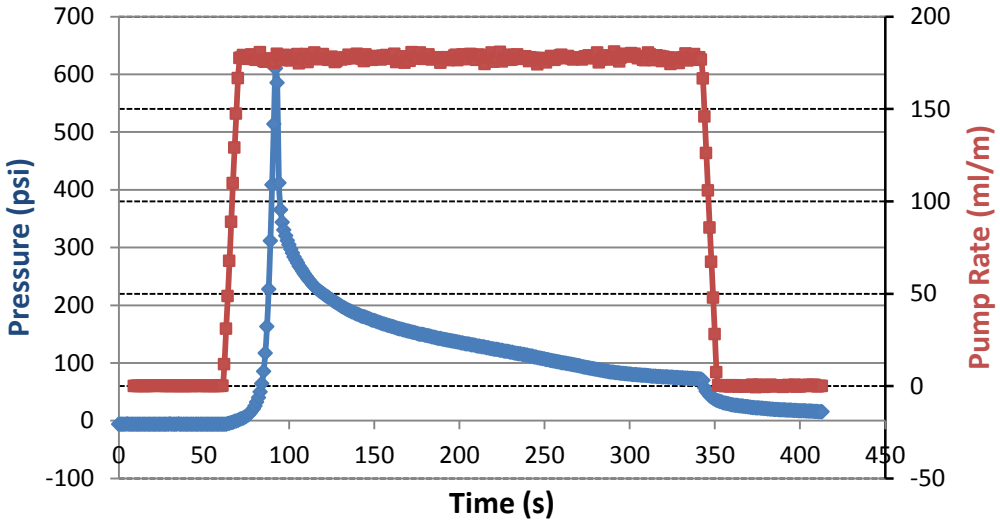

Figure 19. The pump pressure record for the fracture in Figure 13 (Test 1a).

Another example of bypass is illustrated in Figure 20, where a planar fracture propagates around two permeable natural fractures (Berea sandstone slides). The yellow arrows indicate the interpreted direction of the propagation bypassing the natural fractures which are orthogonal to the hydraulic fracture propagation. We see evidence of bypass from the plumose structure seen on the face of the hydraulic fracture. The permeability of the Berea sandstone used was about 100mD whereas the permeability of the gypsum plaster (the host rock) was measured to be 57mD (Table 2). We performed 3 tests with Berea sandstone slides. We set each test up with a similar orientation of natural fractures, but we ran each test at a different horizontal differential stress. The test in Figure 20 was run at 15psi horizontal differential stress, and the other two tests were run at 30psi and 50psi respectively (see Table 3). Bypass in conjunction with separation of weakly bonded interfaces was observed in all three samples.

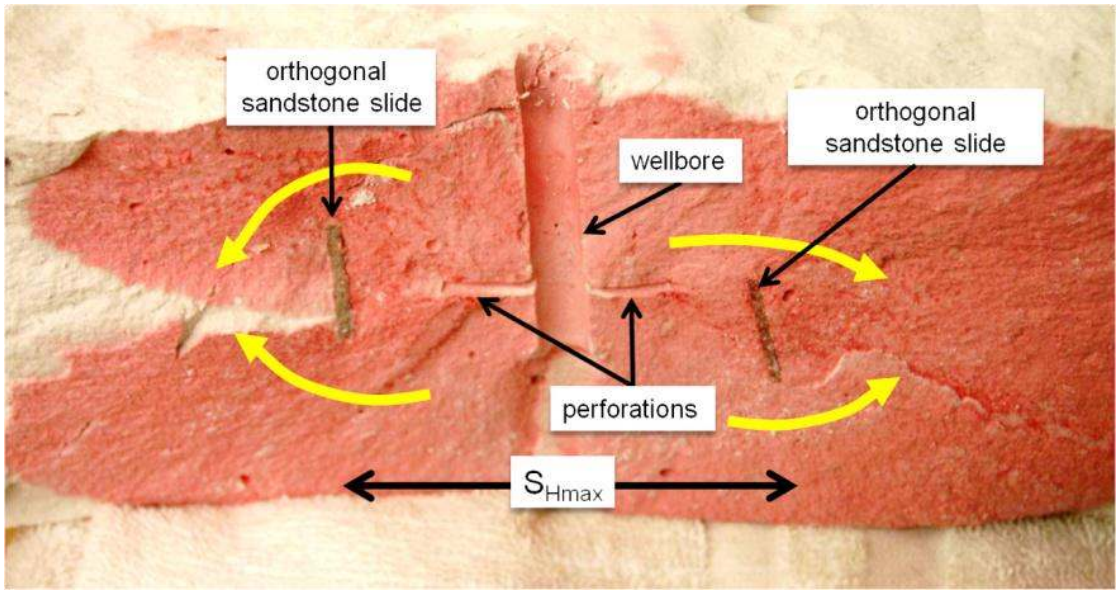

Figure 20. Test 2c exhibiting a hydraulic fracture bypassing two permeable natural fractures (Berea sandstone slides). Yellow arrows indicate interpreted propagation paths. The wellbore is vertical and the main hydraulic fracture propagates in the direction of S_{Hmax} as expected.

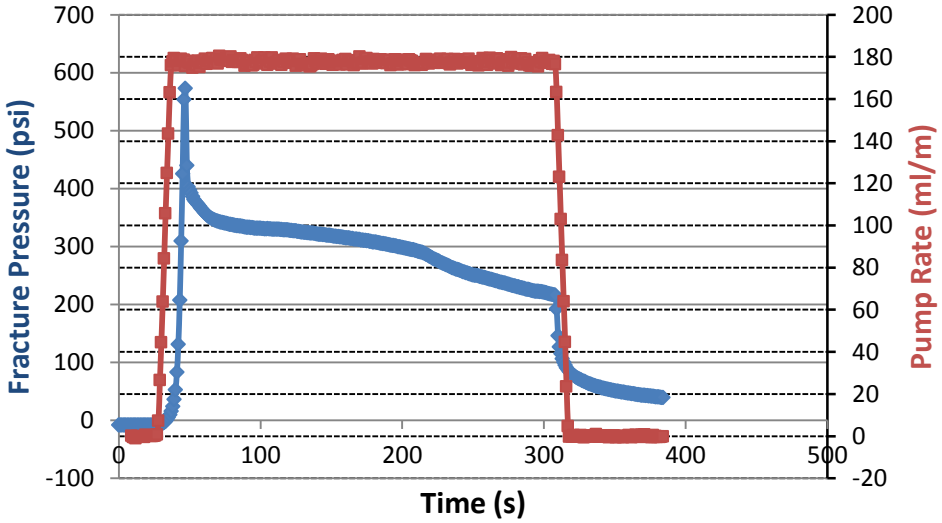

Figure 21. The pump pressure record for the fracture in Figure 20 (Test 2c).

With the exception of tests 1a and 1b, our tests were conducted in a way to constrain the height growth of the vertical hydraulic fractures to a maximum of 4 inches because the middle layer of gypsum plaster was only 4 inches thick. As described in the experimental section, we had two main sizes of natural fractures with one size being taller than the other size. In the height-contained experiments, when we used the taller natural fractures (1.55 in. tall glass or plaster slides) the hydraulic fracture never exhibited pure bypass. In other words, in every case of intersection with a tall natural fracture, there existed some diverted fracture propagation in addition to or instead of bypass. However, when we used the shorter natural fractures (1 in. tall Berea sandstone slides) the hydraulic fracture sometimes exhibited only bypass with separation of the weakly bonded interfaces and other times exhibited a combination of diversion and bypass, but the hydraulic fracture never exhibited pure diversion. This observation suggests that the ratio of hydraulic fracture height to natural fracture height (H_{HF}/H_{NF}) has a strong influence on fracture intersection geometry. The lower the value of H_{HF}/H_{NF}, the more likely a hydraulic fracture is to divert into a new direction of propagation.

BYPASS AND DIVERSION

Bypass and Diversion with Coalescence

In the case of Figure 22 (test 1b – horizontal fracture), the hydraulic fracture propagates into the glass slide at an oblique angle, but the fracture is much wider (taller) than the glass slide, so the fluid-driven fracture can easily bypass around the slide. However, along the intersection line, the fluid keeps flowing between the glass slide and the gypsum plaster (see Figure 22 inset) only along the path leading further from the wellbore (the acute angle path where $|\theta| < 90°$). When the diverted portion of the fracture

following the glass slide reaches the edge of the slide, it kinks along a path that meets up with the bypassing fracture segment, coalescing back into one larger fracture. The inset of Figure 22 also shows that the fluid leaked completely around the perimeter of the glass slide (see the red outline along the top edge of the glass slide), but we don't consider that part of the fracture propagation process. The white portion of the rectangle in the inset indicates the fracture did not grow through that region.

This observation (that the hydraulic fracture diverted along the natural fracture in only one direction) supports work done by Dahi-Taleghani and Olson (2011) which shows that a hydraulic fracture is likely to propagate in only one direction for non-orthogonal intersections with cemented fractures, following the path of maximum energy release rate, which occurs along the path moving further away from the pre-existing pressurized fracture (the acute angle path). This test was the only sample containing an intersection where the hydraulic fracture opened up the weakly bonded interface between the natural fracture and the host rock in only one direction (see the inset in Figure 22). It is not clear why we only observed this phenomenon in this sample and not in other samples, but possibly the rigidity and impermeability of the glass allows interfacial separation in only one direction. We hope to understand this type of fracture geometry more with future tests.

The pressure record for this test is displayed in Figure 23. The horizontal orientation of the wellbore in conjunction with slightly deviated perforations (titled towards the horizontal plane) could have caused the hydraulic fracture to initiate horizontally. Often during a fracturing test, the fracturing fluid fills up the annulus by separating the bond between the gypsum cement and the wellbore. If the wellbore annulus is invaded before fracture initiation, the orientation of the wellbore might determine the orientation of the hydraulic fracture considering our tests have high net

pressures (see fracture pressure value compared to S_{hmin} in Figure 23). Most of our tests were conducted with a vertical wellbore (see Table 3). None of the tests with vertical wellbores produced a horizontal fracture where as one of the two tests we conducted with horizontal wellbores produced a horizontal fracture.

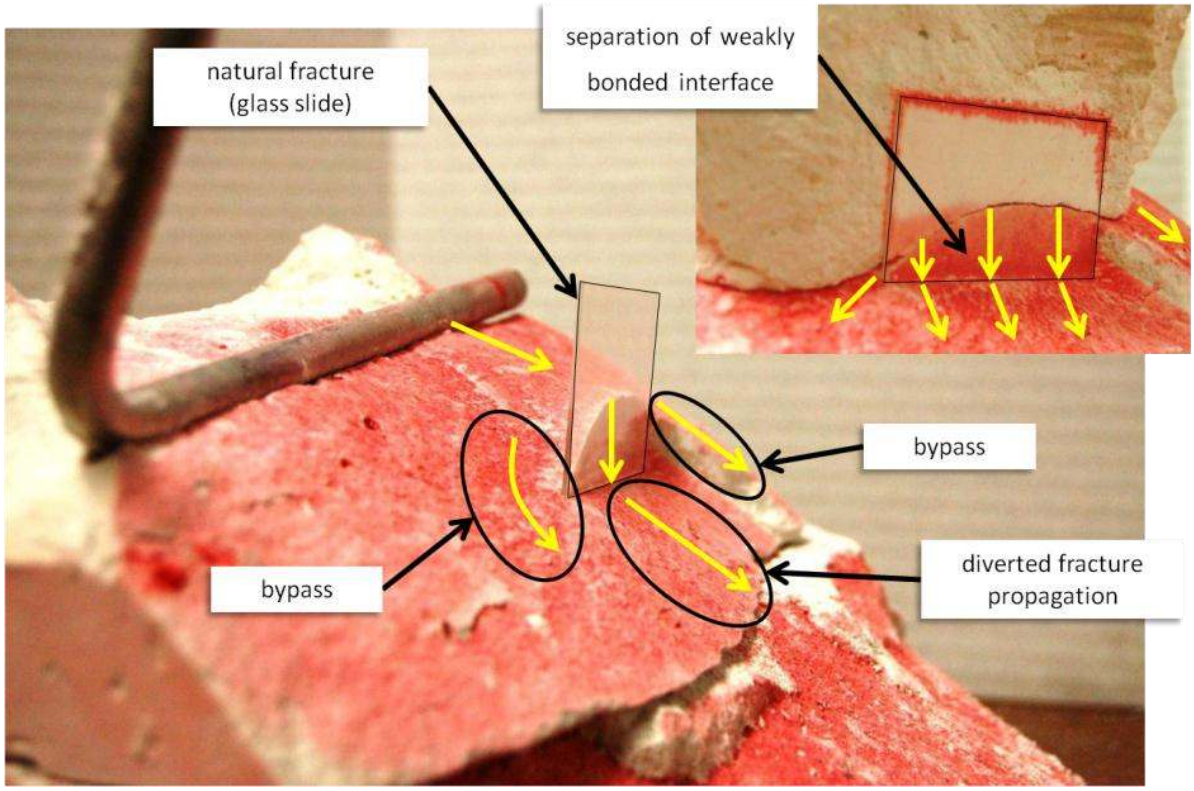

Figure 22. Test 1b exhibiting complex propagation paths with bypass around glass slide as well as diverted fracture propagation (inset shows that interfacial separation only happens in the direction away from the wellbore). The bypassed and diverted paths meet up on other side of glass slide away from wellbore. Wellbore placed parallel to the direction of S_3 (S_{Hmin}). The main hydraulic fracture propagated horizontally (perpendicular to S_1) which was unexpected.

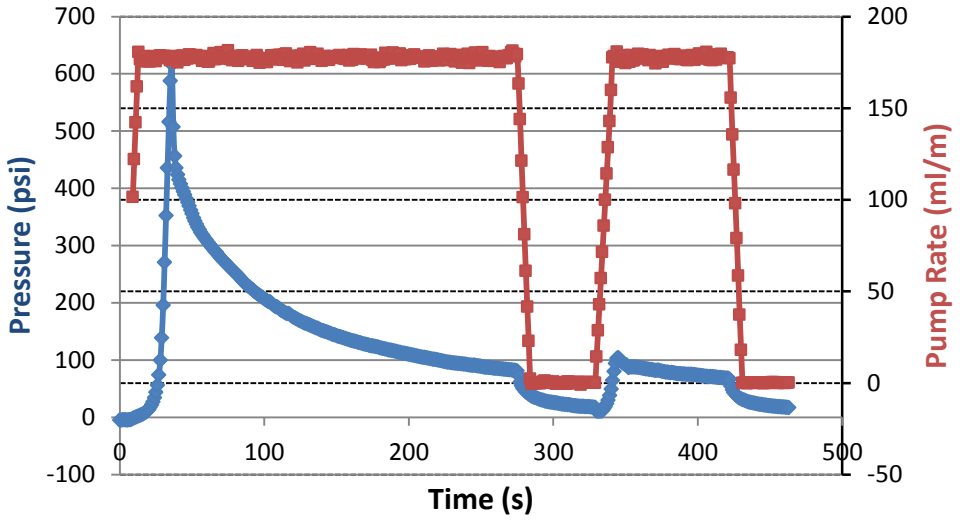

Figure 23. The pump pressure record for the fracture in Figure 22. The brief shutdown about about 280 seconds was to refill the pump with an additional half liter for fracture fluid in an attempt to propagate a larger fracture.

Bypass and Diversion without Coalescence

In Test 1c, there was initial bi-wing propagation from the wellbore. In one direction was an obliquely oriented natural fracture and in the other was an orthogonally oriented one. In the oblique case (Figure 24), a complex intersection geometry developed involving bypass and diverted propagation kinking off of one end of the natural fracture (glass slide). The hydraulic fracture is taller than the natural fracture which allows for the bypass underneath (see Figure 25 for a closer view of the full hydraulic fracture face). The angle of intersection can be seen from the inset to be acute where $\theta = 60°$. The inset shows the angle to be 120°, but that is not the angle of intersection (θ) as we defined it (see Figure 13). As seen, the hydraulic fluid separates the weakly bonded interface between the glass slide and the gypsum plaster in both directions after intersection. However, the propagation only continues from the end of the natural fracture that is located farthest away from the wellbore.

As shown in Figure 25, the hydraulic fracture bypasses in the lower portion (beneath the glass slide) but diverts obliquely in the upper portion (above the glass slide). This might be due to the placement of the perforations. Since the perforations were placed on the bottom of the gypsum plaster layer (Figure 25), the fracturing fluid most likely began to bypass beneath the glass slide before the fluid even reached the glass slide. By the time the fluid reached the upper edge of the glass slide, a portion of the fluid flow was likely already diverted down the glass slide which made the hydraulic fracture divert obliquely (away from the wellbore, $\theta = 60°$) instead of bypassing above the glass slide. The pump record for this test is shown in Figure 26.

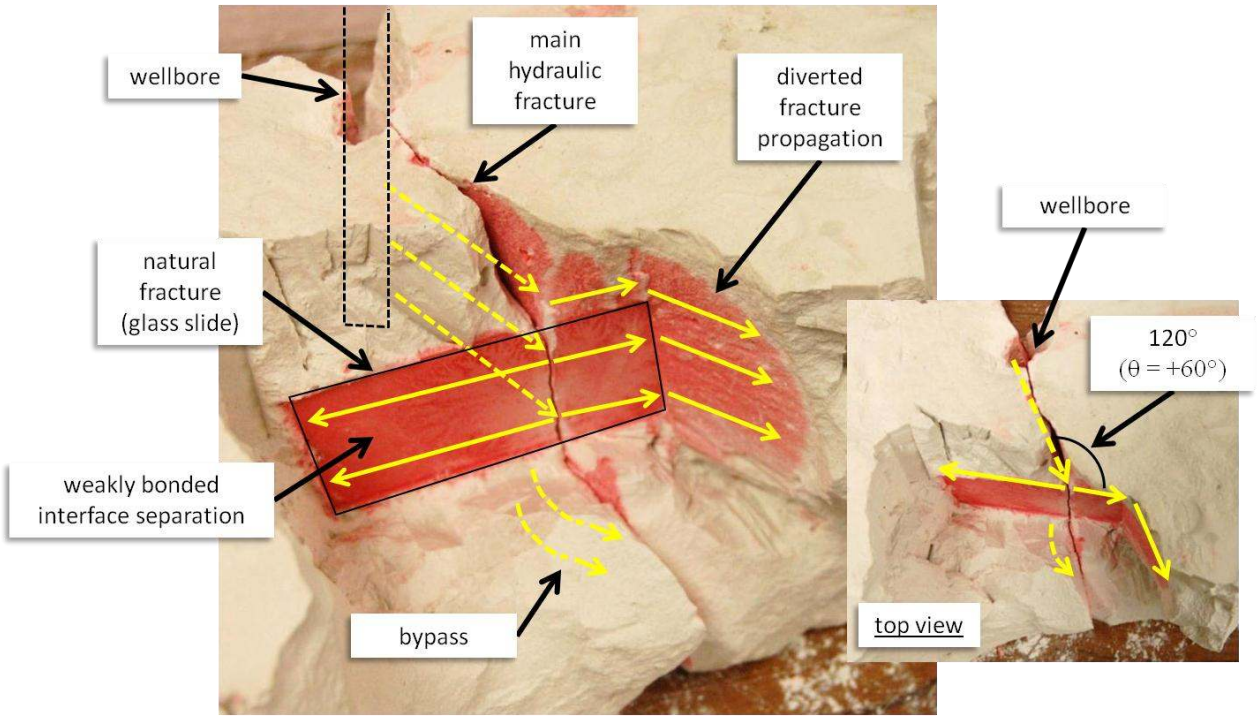

Figure 24. Test 1c exhibiting complex vertical propagation paths including bypass around glass slide as well as diverted fracture propagation. The inset shows a top view of the hydraulic fracture so the angle of intersection ($\theta = 60°$) can be easily seen. The wellbore is vertical and the main hydraulic fracture propagates in the direction of S_{Hmax} as expected.

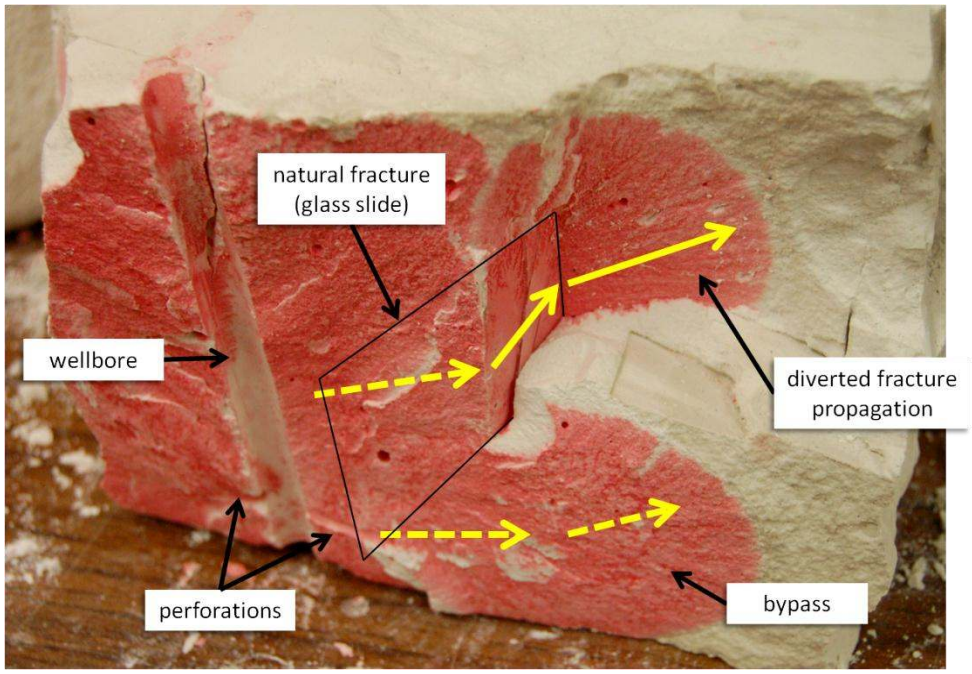

Figure 25. Test 1c exhibiting a zoomed in view of the diverted fracture propagation and the bypass. This is the same fracture intersection that is shown in Figure 17 except the fracture face is exposed to show the bypass.

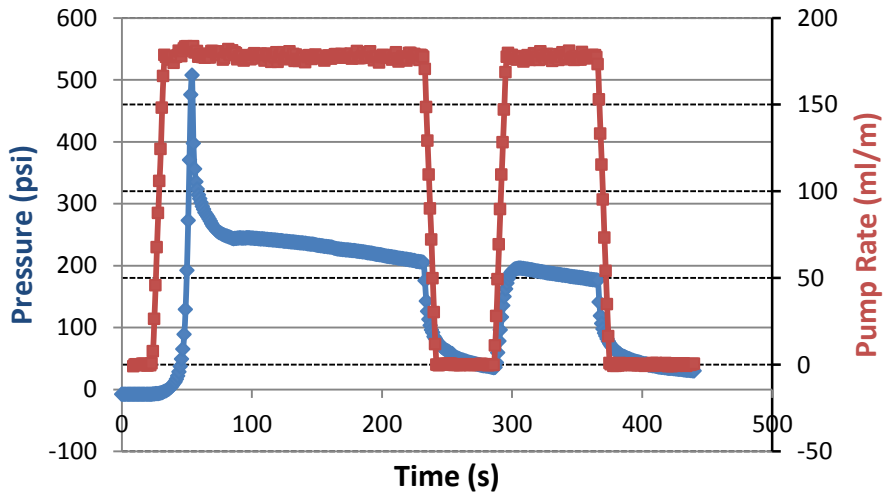

Figure 26. The pump pressure record for the fractures shown in Figure 24, Figure 25, and Figure 27 (Test 1c).

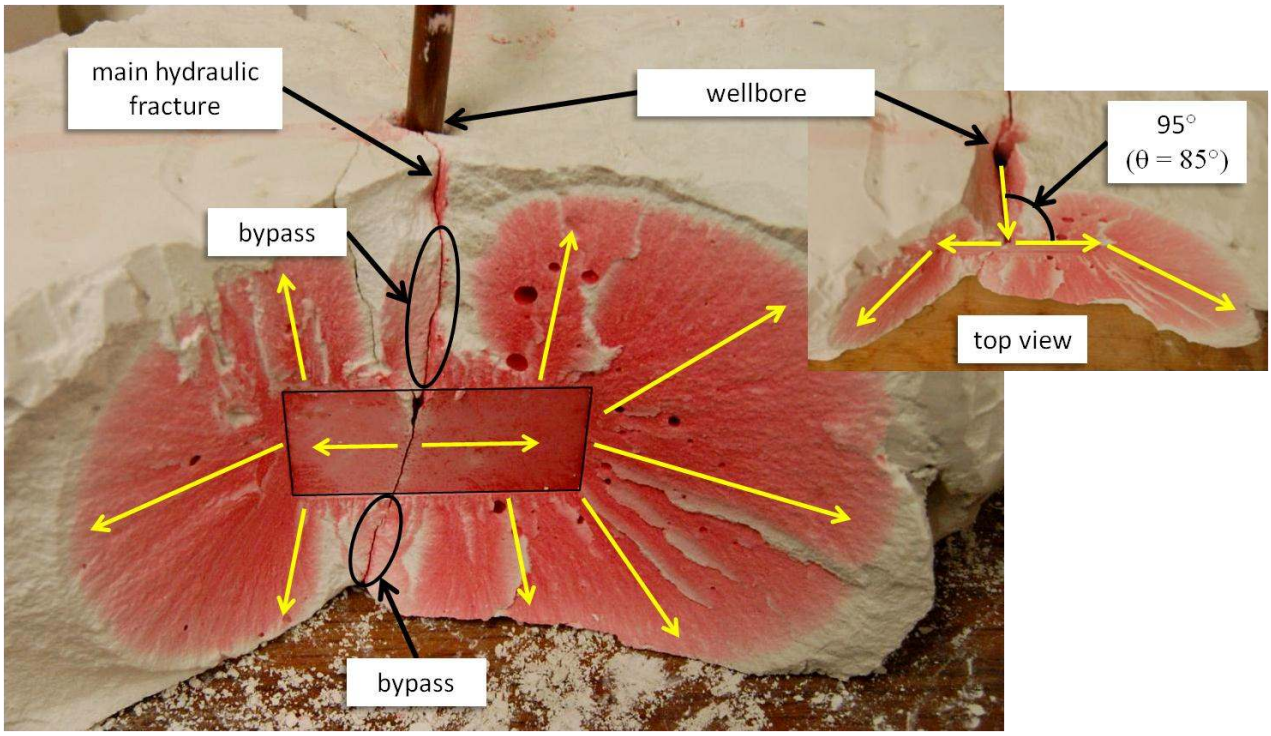

Figure 27. Test 1c exhibiting complex propagation paths including bypass above and below the glass slide as well as diverted fracture propagation off of all four edges of the glass slide which is roughly orthogonal to the direction of the main hydraulic fracture. The inset shows a top view of the hydraulic fracture so the angle of intersection ($\theta = 95°$) can be easily seen. The wellbore is vertical and the main hydraulic fracture propagates in the direction of S_{Hmax} as expected.

In the orthogonal case for Test 1c, the complex propagation involved bypass above and below the glass slide as well as diverted fracture propagation kinking off all four edges of the glass slide (Figure 27). The inset of the figure shows a top view of the hydraulic fracture indicating the angle of intersection ($\theta = 95°$). It is interesting to note that the fracture geometries for lateral propagation from the vertically oriented natural fracture tips and vertical propagation from the horizontally oriented natural fractures tips have very different geometric character, exemplifying mixed mode I-II and mixed mode I-III (Figure 28), respectively (Cooke and Pollard, 1996).

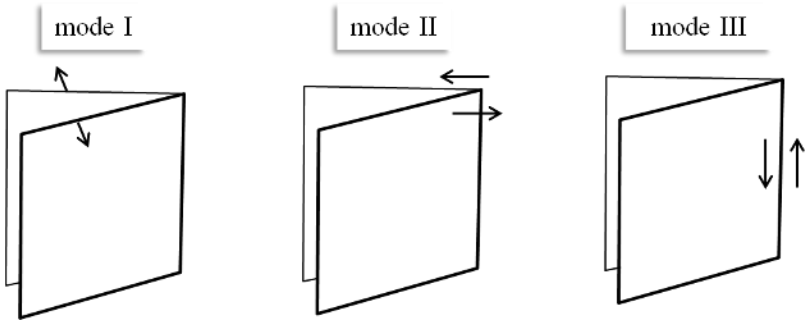

Figure 28. A depiction of the three types of crack propagation modes. Mode I is tensile loading while mode II and mode III are shear loading.

The mixed mode I-II case is illustrated in Figure 29a, which is a diagrammatic depiction of the fracture in Figure 29b. The red arrows shown on the intersection indicate the shear that is caused by the opening mode crack (main hydraulic fracture). The open crack displacement due to P_{net} in the fracture causes a shear to be applied across the natural fracture (the crack opening is greatly exaggerated for explanation purposes). The front face of the glass slide (weakly bonded interface) is separated by the diverted hydraulic fluid shown in yellow, but the backside face of the glass side is still bonded to the host rock. This is how the shear caused by the opening mode crack is applied across the natural fracture (glass slide). Notice that the shear is applied in opposite directions on either side of the hydraulic fracture / natural fracture intersection. The zoomed-in portion of Figure 29a shows how this shear acts at the right edge of the glass slide. The crack front at the right edge of the glass slide is perpendicular to the shear, so this type of fracture propagation is mixed mode I-II.

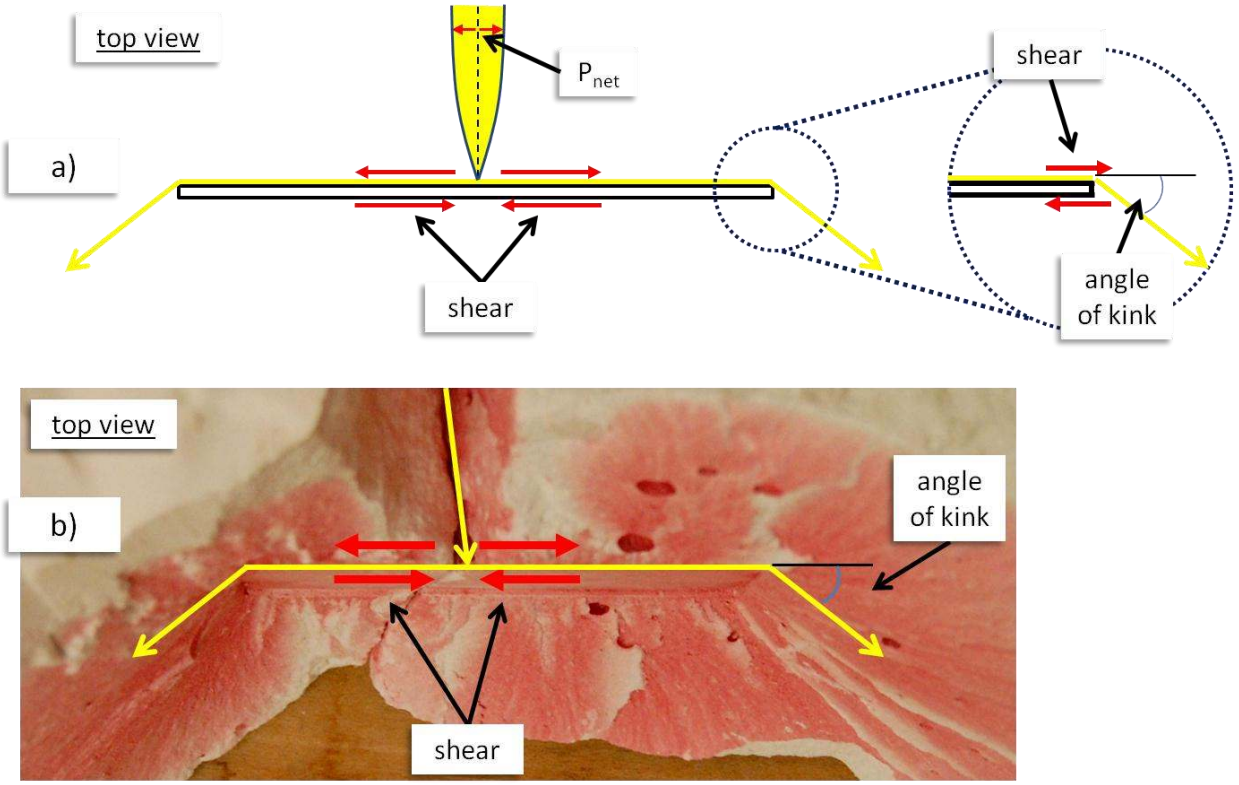

Figure 29. Part a) depicts a top view sketch of the hydraulic fracture shown in Figure 20. The red arrows show the shear on the natural fracture plane due to the opening of the perpendicular hydraulic fracture. The hydraulic fracture is shown in yellow and the hydraulic fracture crack width is greatly exaggerated for visual purposes. The zoomed portion of part a) shows how the shear is applied perpendicular to the crack front at the right edge of the glass slide. Part b) shows a top view of the fracture intersection in Figure 20 (Test 1c).

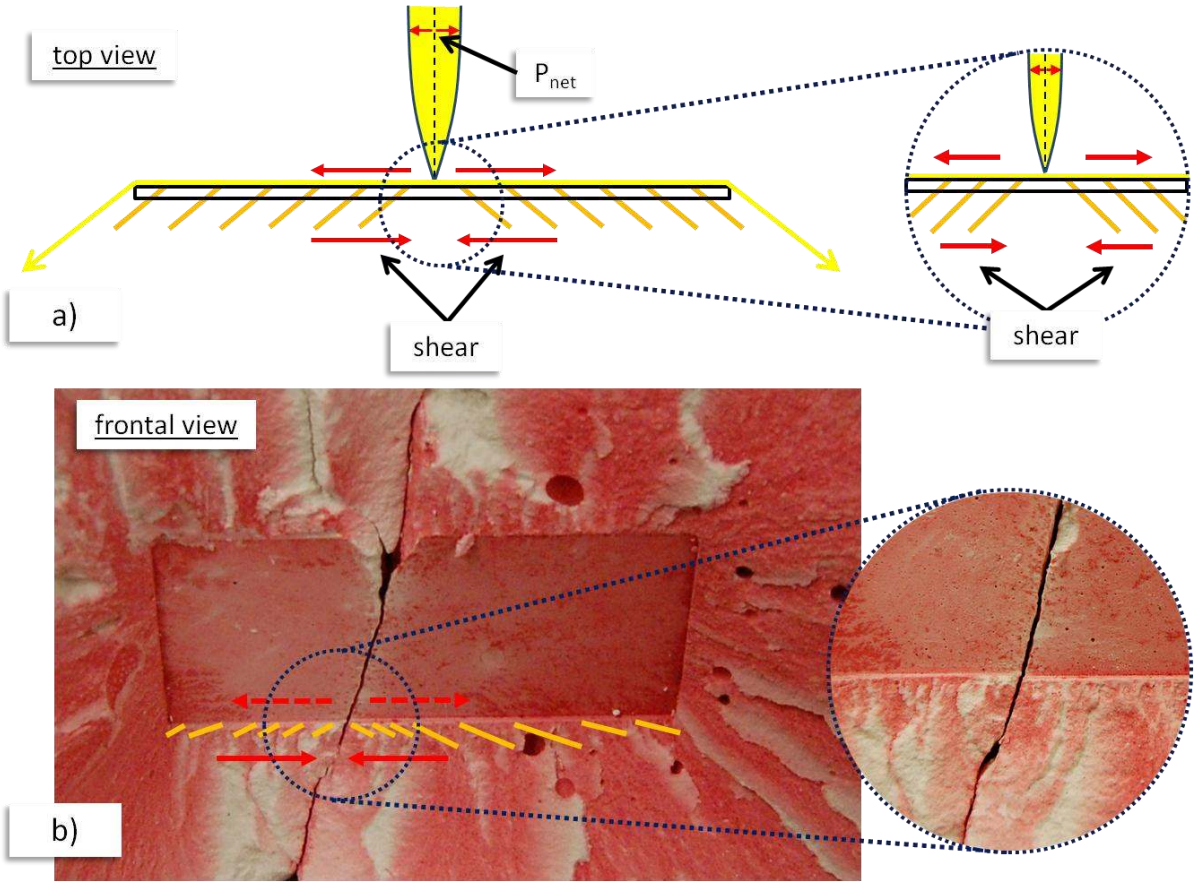

Figure 30. Part a) depicts an idealized top view sketch of the fracture intersection shown in Figure 20 (Test 1c). The red arrows show the shear applied on the crack plane parallel to the crack front. Part b) shows a frontal view of the actual hydraulic fracture / natural fracture intersection. The zoomed portion of part b) shows en echelon cracks that propagate in a mixed mode I-III fashion. Looking closely, one can tell that the cracks propagate in mirror image directions on either side of the hydraulic fracture / natural fracture intersection line according to the shear.

Propagation from the top and bottom edges of the glass slide is depicted diagrammatically in Figure 30a for the fracture close-up in 23b. Similar to that displayed in Figure 29a, the hydraulic fracture / natural fracture intersection imposes opposite senses of shear on either side of the hydraulic fracture tip, but now that shear is acting parallel to the top and bottom of the slide in a mode I-III fashion (Figure 30a). The red

arrows show the shear applied on the crack plane parallel to the crack front. The angled parallel lines indicate the twisting of vertically propagating en echelon cracks coming off the bottom edge of the natural fracture (into the page). The sense of rotation of the en echelon fractures is reverse from one side of the intersecting hydraulic fracture plane to the other. Looking at the experimental block (Figure 30b), the en echelon cracks also propagate off of the top of the natural fracture. As these fractures propagate away from the glass slide edge downward, they eventually start to coalesce, such that the number of fracture segments reduces with added propagation.

The fracture intersection geometry in Test 3a (Figure 31) was very similar that in Test 1c (Figure 30) even though the natural fractures were completely different (Test 1c contained glass slides and Test 3a contained plaster slides). In general, the types of intersection geometries we observed did not seem to be functions of the natural fracture composition. Rather, the intersection geometries we observed were functions of angle of hydraulic fracture / natural fracture intersection, H_{HF}/H_{NF}, and the horizontal differential stress.

Figure 31. Test 3a exhibiting a roughly orthogonal intersection between a hydraulic fracture (propagating out of the page) and a plaster slide (seen by the rectangular outline). There is mode I-II propagation to the right and left of the natural fracture, and there is mode I-III propagation above and below the natural fracture. As seen, the mode I-III en echelon cracks propagate in directions that are mirror images of each other across the hydraulic fracture / natural fracture line of intersection.

NET PRESSURE

High net pressure can be seen in all of our fracturing test pressure records. As seen in Figure 16 and Figure 21, the wellbore pressure is very high compared to the principal stresses. The fracture propagating pressure is between 200psi and 300psi in these tests which is much higher than even the maximum principal stress (S_v = 100psi).

This high net pressure ($P_{frac} - S_{Hmin}$) means that the fracture intersection geometries that we observe are most likely biased towards emphasizing the effects of net pressure over the effects of horizontal differential stress. Most likely, we would observe

less fracture diversion and more fracture bypass in tests where the differential stress was higher and the net pressure was lower. Fracture bypass is more likely when the horizontal differential stress is higher because the higher horizontal differential stress makes it harder for a hydraulic fracture to propagate in a direction that is not parallel to S_2 (S_{Hmax} for vertical fractures). Even though our tests are biased towards the effects of net pressure, we know that our tests still include the effect of differential pressure because we observed that fracture diversion was more likely when we had lower differential stress. In addition, eight of our nine experiments showed the fracture initiating in the expected direction (+/- 10°) indicating that the effect of high net pressure is not overshadowing the effect of the horizontal differential stress.

In Figure 19, the fracture propagating pressure is between 75psi and 200psi which is lower than it is in Figure 16 and Figure 21. This is because Figure 19 shows an experiment where the hydraulic fracture was not contained in height. Hydraulic fractures become more compliant as the fracture height increases, which lowers the fracture propagating pressure. Accordingly, all of our height-contained fractures maintained high fracture propagation pressure as seen in Figure 16 and Figure 21. One way that we intend to lower the fracture propagation pressure in the future is by pumping slower, but we have had some fracture initiation problems when pumping at lower rates. In addition, the fracturing fluid tended to easily come up the wellbore annulus by separating the wellbore from the host rock when we pumped slower.

CROSSING OF NATURAL FRACTURES

Theoretically, hydraulic fractures should be able to propagate through (cross) natural fractures and continue without having to bypass the natural fracture or divert

down it. Blanton (1982) showed that a hydraulic fracture can cross a frictional interface when the differential stress is high and the angle of approach is high (near orthogonal). In our experiments with cemented natural fractures, the hydraulic fracture would have to break the natural fracture cement in order to cross.

Natural fracture cement strength is an important property to consider because the hydraulic fracture is more likely to cross a cemented natural fracture if the cement tensile strength is low compared to the host rock tensile strength. We have considered the case in which the cement is stronger than the host rock (glass slides in gypsum plaster host rock and sandstone slides in gypsum plaster host rock). This case would be analogous to a field case in which low strength shale contained natural fractures filled with high strength quartz cement. We have also considered the case in which the cement has the same tensile strength as the host rock (gypsum plaster slides in gypsum plaster host rock). We have not performed tests where the natural fracture cement is weaker than the host rock, but we plan to do this with future work. So far, we have found little evidence of a hydraulic fracture breaking apart the cement that fills the natural fracture in order to cross it. Our experiments show that bypass in conjunction with the separation of weakly bonded interfaces is a much more likely scenario than crossing for cemented natural fractures especially if H_{HF}/H_{NF} is large (which is likely in the field if the main natural fractures are joints).

Natural fractures (joints) may range in length from a few meters up to several hundred meters in rare cases. Joints may span many layers (perpendicular to bedding planes), but they rarely exceed several tens of meters in height (Pollard and Aydin, 1988). However, hydraulic fractures range in height from a hundred feet up to as much as two thousand feet (Fisher and Warpinski, 2012). Therefore, H_{HF}/H_{NF} is most likely very large for most hydraulic fracture / natural fracture intersections unless the natural fractures are

faults, not joints. Joints are mode I fractures which are generally confined by bedding planes, but faults are not necessarily confined by bedding planes and may measure thousands of feet in height. In a given reservoir, faults are likely to be fewer in number compared to the number of joints (Pollard and Aydin, 1988). Following this logic, we think that in most reservoirs, the bulk of the hydraulic fracture / natural fracture interactions will be between hydraulic fractures and joints. If this is the case, H_{HF}/H_{NF} will most likely be large for most fracture interactions and bypass should be an important propagation mechanism in real fracture stimulation treatments. Such a fracture intersection geometry would require a true 3d analysis for modeling.

Although intersections between hydraulic fractures and joints are probably more common, intersections between hydraulic fractures and faults might be more likely to cause complex diversion since H_{HF}/H_{NF} is likely to be smaller in these cases. As we have found in our experiments, the lower the ratio of H_{HF}/H_{NF} the more likely the fracture is to exhibit diverted fracture propagation.

Another important aspect to consider when examining hydraulic fracture crossing is the strength of the bond between the cement that fills the natural fracture and the host rock. In order to communicate stress across an embedded natural fracture, there must be some bond strength between the cement and the host rock. Therefore, a stronger bond between natural fracture and host rock would help hydraulic fracture crossing. As discussed in the experimental setup section, we used modified SCB tests to measure the plaster-plaster bond toughness and to estimate the Berea-plaster bond toughness and the glass-plaster bond toughness. The glass slides have a relatively weak bond to the gypsum plaster, and the gypsum plaster slides and the Berea sandstone slides have a relatively strong bond to the gypsum plaster host rock.

In our experiments, the test most likely to contain crossing was Test 3a. Test 3a had the highest differential stress of our tests (50psi) and the weakest natural fracture (plaster) with the strongest bond to the host rock (plaster-plaster). However, even in Test 3a, the intersection between a hydraulic fracture and an orthogonal plaster natural fracture did not result in crossing. To determine why we did not observe fracture crossing in any of our experiments, we considered the 2D crossing criterion described below.

When a propagating hydraulic fracture reaches a certain distance from a natural fracture, the natural fracture will fail in tension orthogonal to the propagation direction and allow the hydraulic fracture to cross if the tensile stress is great enough to break the natural fracture. However, the natural fracture will not break in tension if the natural fracture / host rock bond has already failed in tension or shear. In our experiments with gypsum plaster natural fractures, the natural fractures are the same material as the host rock. In this case, r_p (the radius of the process zone) is the distance at which a natural fracture will fail in tension orthogonal to S_{Hmax} (allowing crossing) if no shear failure or tensile failure has occurred already on the natural fracture / host rock bond.

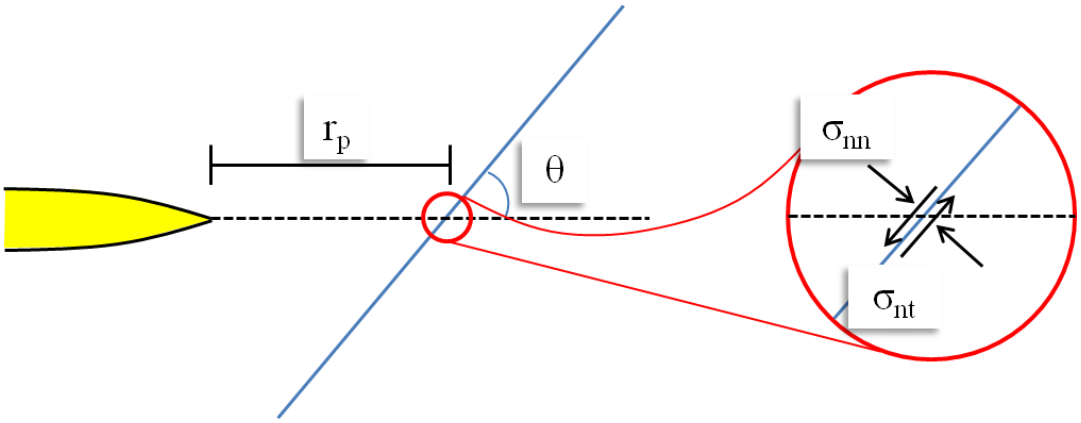

Figure 32. The crossing criterion with angle of intersection (θ). The hydraulic fracture (shown in yellow) is at a distance of r_p (the radius of the process zone) away from intersecting the natural fracture at the point in line with the hydraulic fracture direction (circled in red).

As shown in Figure 32, we are concerned with the point on the natural fracture that is directly in front of the approaching hydraulic fracture because this is the point at which natural fracture / host rock bond failure will result in diversion of the hydraulic fracture instead of crossing. Assuming compressive stress is positive, bond tensile failure will occur when the effective normal stress acting on the bond (σ_{nn}) is less than (more tensile than) the bond strength ($-T_{bond}$), as

$$-\sigma_{nn} > T_{bond} \,, \qquad \text{Eq. 7}$$

the bond shear failure criterion is

$$|\sigma_{nt}| > S_{0,bond} + \mu_{i,bond}\sigma_{nn} \,, \qquad \text{Eq. 8}$$

where $S_{0,bond}$ is the bond cohesion and $\mu_{i,bond}$ is the bond friction coefficient.

The normal stress on the natural fracture is calculated as the addition of the stress induced by the fracture tip (near-tip stress) and the far field stress. The near-tip stresses are calculated using the method outlined by Lawn and Wilshaw (1975). The near-tip stress at the point of interest is isotropic directly in front of the mode I fracture tip. The far field stress normal to the natural fracture is calculated by using a 2D stress resolution

equation (Zoback, 2007). Assuming compressive stress is positive, the resulting equation for the normal stress on the natural fracture at the point directly in front of the fracture tip is

$$\sigma_{nn} = \frac{-K_I}{\sqrt{2\pi r_p}} + S_{Hmax}\cos^2\left(\frac{\pi}{2} - \theta\right) + S_{Hmin}sin^2\left(\frac{\pi}{2} - \theta\right). \quad \text{Eq. 9}$$

The near-tip shear stress directly ahead of a mode I crack is 0. The far field shear stress on the natural fracture is calculated by using a 2D stress resolution equation. The resulting equation for the shear stress on the natural fracture at the point directly in front of the hydraulic fracture is

$$\sigma_{nt} = (S_{Hmax} - S_{Hmin})sin\left(\frac{\pi}{2} - \theta\right)cos\left(\frac{\pi}{2} - \theta\right). \quad \text{Eq. 10}$$

In order to calculate the whether or not crossing should occur given a certain differential stress and angle of intersection (θ), we need to know T_{bond} (Eq. 7), $S_{0,bond}$ (Eq. 8), K_I (Eq. 9), r_p, and μ. We assume that the fracture is propagating at the critical stress intensity factor ($K_I = K_{Ic}$), and we estimate the plaster-plaster frictional coefficient (μ) to be 0.6. We calculate r_p by assuming that neartip stress equals the tensile strength as

$$r_p = \frac{{K_{Ic}}^2}{2\pi(T_{rock}+S_{Hmin})^2}. \quad \text{Eq. 11}$$

We estimate T_{bond} and $S_{0,bond}$ by multiplying the intact rock tensile strength and cohesion by a cement bond factor (C_{cb}) where C_{cb} is between 0 and 1, given by

$$T_{bond} = C_{cb}T_{rock} \quad \text{Eq. 12}$$

$$S_{0,bond} = C_{cb}S_{0,rock}. \quad \text{Eq. 13}$$

If C_{cb} is equal to 1, the natural fracture / host rock bond is just as strong as the intact host rock. Using the fracture toughness measurements from Table 4 and Table 5, C_{cb} can be estimated as

$$C_{cb} = \frac{K_{Ic,bond}}{K_{Ic,rock}} = \frac{0.1(\text{MPa}\sqrt{\text{m}})}{0.12\ (\text{MPa}\sqrt{\text{m}})} = 0.833. \quad \text{Eq. 14}$$

Our calculated C_{cb} is an estimate that provides us an idea of how likely crossing should be in our experiments with plaster natural fractures. Basing the bond tensile strength and cohesion off of C_{cb} allows us to easily see how a weaker or stronger bond affects crossing by adjusting C_{cb}. Gypsum plaster tensile strength is 294 psi (Table 2) and the internal cohesion (S_0) of gypsum plaster calculated from the UCS value and μ_i is 214.5 psi. Our calculated C_{cb} of 0.833 gives us a tensile bond strength (T_{bond}) of 245 psi and a bond cohesion ($S_{0,bond}$) of 179 psi.

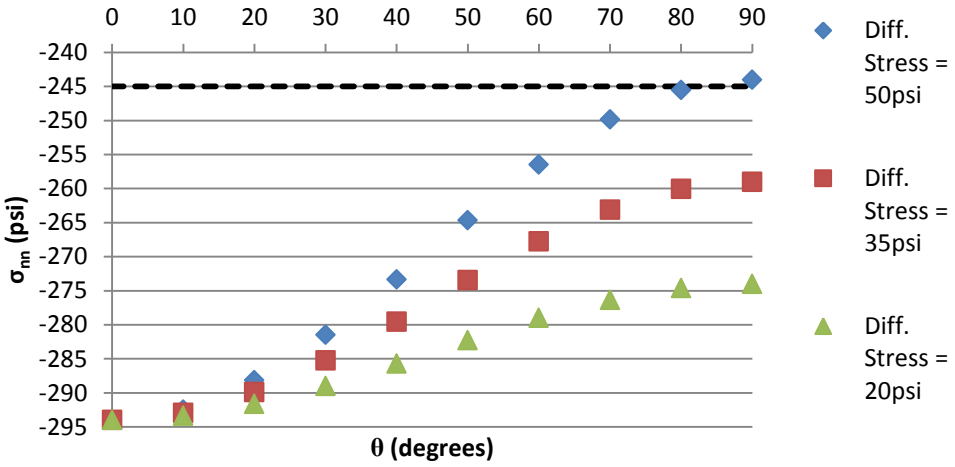

Figure 33. A plot of normal stress on natural fractures with different angles of intersection (compression is positive). The three different sets of points have different horizontal differential stress values as shown in the legend. The dashed line represents the estimated tensile strength of the plaster-plaster bond (245 psi).

Figure 33 shows a plot of normal stress on natural fractures of different angles of intersection (compression is positive). The three different sets of points have different horizontal differential stress values as shown in the legend. These three differential stresses (50psi, 35psi, and 20psi) are equivalent to the differential stresses in tests 3a, 3b, and 3c respectively. The dashed line represents the estimated tensile strength of the

plaster-plaster bond (245 psi). If a point falls below the dashed line, then the tensile crossing criterion equation (Eq. 7) predicts that the natural fracture bond will fail in tension before the hydraulic fracture reaches a distance of r_p from the natural fracture which will prevent crossing. Assuming our estimated bond strength is accurate, Figure 33 shows that no crossing should occur except at the highest differential stress (50psi) and the highest angle (90°). This explains why we do not see crossing in most of our experiments.

In Test 3a (plaster natural fractures, differential stress of 50psi), we observed an orthogonal intersection between a natural fracture and a hydraulic fracture that did not result in crossing as predicted in Figure 33. This could be due to the fact that the experiment allows for bypass which is not accounted for in this 2D crossing criterion.

Now that we have determined why we do not observe crossing in our experiments, let us examine the likelihood of crossing in experiments of higher stress. As discussed in the scaling section, our experiments are scaled such that the lab to field ratio of the confining stress dimensionless group is 0.4. In order to obtain a confining stress dimensionless group ratio of 1, our tests would have to be performed with a confining stress (S_{Hmin}) of 125 psi.

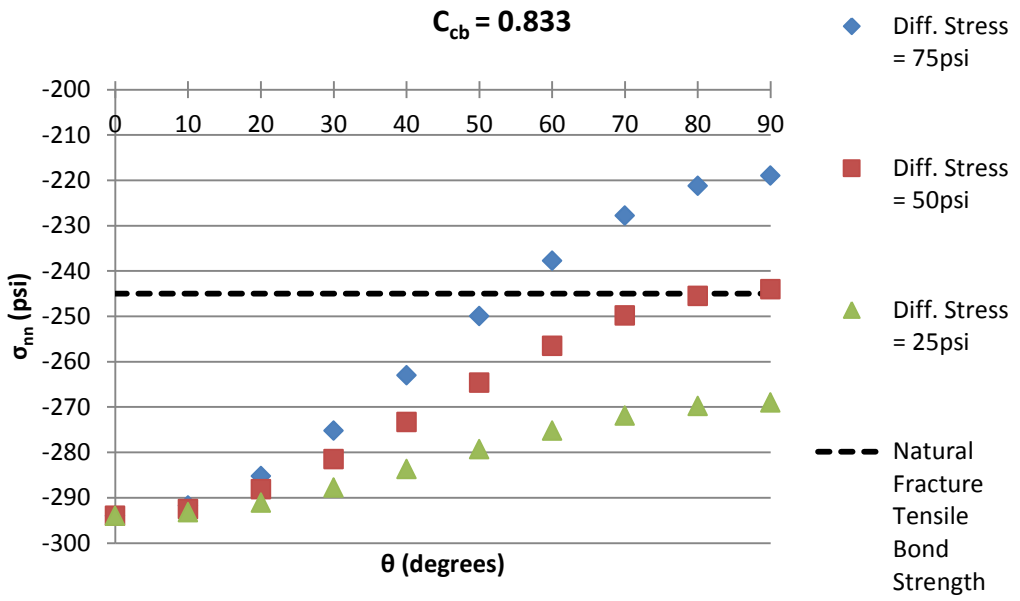

Figure 34. Normal stress on natural fractures is plotted vs. angle of intersection for a strong cement bond (C_{cb} = 0.833, compression is positive). The three different sets of points have different horizontal differential stress values as shown in the legend. The dashed line represents the estimated tensile strength of the plaster-plaster bond (245 psi).

Figure 34 was generated with appropriately scaled confining stress (S_{Hmin} = 125 psi) and higher differential stress (25psi, 50psi, and 75psi). The dashed line represents the estimated tensile strength of the plaster-plaster bond (245 psi). If a point falls below the dashed line, then the tensile crossing criterion equation (Eq. 7) predicts that the natural fracture bond will fail in tension before the hydraulic fracture reaches a distance of r_p from the natural fracture which will prevent crossing. Assuming a cement bond factor (C_{cb}) of 0.833, Figure 34 shows that crossing will not occur at all when the differential stress is 25 psi. However, Figure 34 also shows that crossing should occur when $\theta > 85°$ for a differential stress of 50 psi, and that crossing should occur when $\theta > 55°$ for a differential stress of 75 psi. If the cement bond factor (C_{cb}) is smaller, the likelihood of crossing dramatically decreases.

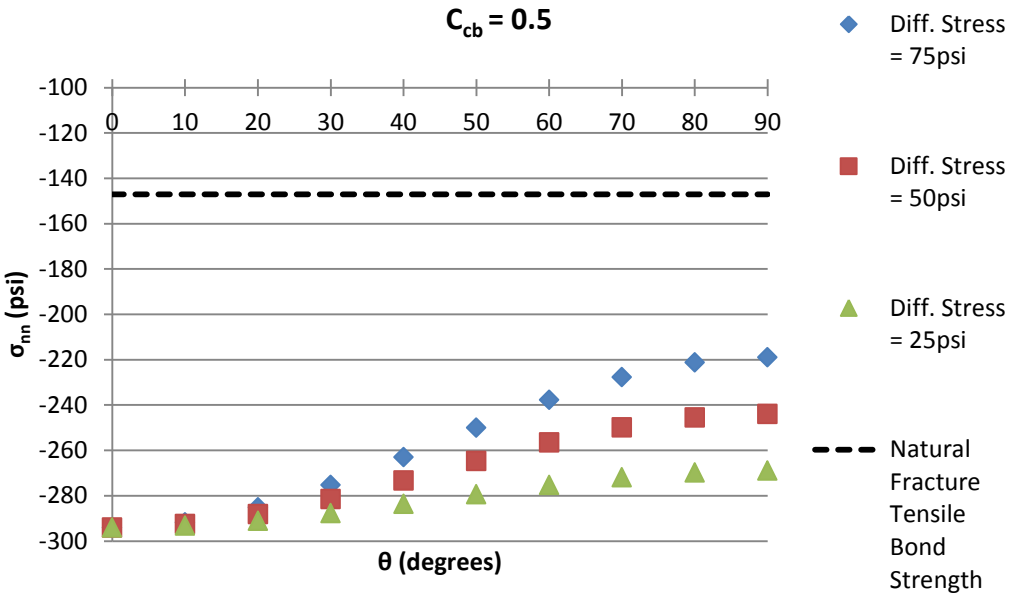

Figure 35. Normal stress on natural fractures is plotted vs. angle of intersection for a weaker cement bond (C_{cb} = 0.5, compression is positive). The three different sets of points have different horizontal differential stress values as shown in the legend. The dashed line represents the estimated tensile strength of the plaster-plaster bond (147 psi).

Figure 35 was generated with appropriately scaled confining stress (S_{Hmin} = 125 psi) and higher differential stress (25psi, 50psi, and 75psi). The dashed line represents the natural fracture bond tensile failure criterion. If a point falls below the dashed line, then the tensile crossing criterion equation (Eq. 7) predicts that the natural fracture bond will fail in tension before the hydraulic fracture reaches a distance of r_p from the natural fracture which will prevent crossing. Due to the lower cement bond factor (C_{cb} = 0.5), crossing should not occur at any angle or differential stress. A comparison between Figure 35 and Figure 36 illustrates the strong effect of cement bond strength. A weaker bond allows differential stress to play a greater role in preventing or allowing crossing.

IMPLICATIONS FOR MODELING COMPLEX HYDRAULIC FRACTURE NETWORKS

Today's hydraulic fracturing models do not take into account the complexity of hydraulic fracture / natural fracture interactions. Olson (2008) presents a pseudo-3D fracture model based on fracture mechanics governing equations which is capable of predicting hydraulic fracture / natural fracture interactions. Weng et. al. (2011) presents another pseudo-3D fracture model that uses an analytical crossing model to predict hydraulic fracture / natural fracture interactions, and also takes into account the issue of fluid flow and proppant transport in a complex fracture network . The Weng et al. (2011) analytical crossing model (adapted from work done by Renshaw and Pollard, 1995) assumes that there are four outcomes in the intersection between a hydraulic fracture and a natural fracture. These four outcomes are crossing, arresting, branching, and reinitiating with an offset. Renshaw and Pollards work (1995) and Blanton's work (1882) assume that natural fractures are frictional interfaces that span the entire height of the contained hydraulic fracture. In these scenarios, bypass is not possible because the natural fractures span the entire height of the contained hydraulic fracture. However, our results indicate that bypass is likely to happen in the field and that a more realistic model of hydraulic fracture / natural fracture intersection geometry would include bypass and diversion with mode I-II and mode I-III types of propagation. These types of complex interactions can only be modeled with a full 3D modeling solution.

Conclusions

Physical experiments such as these can provide insight into interactions between natural and hydraulic fractures for various interaction geometries. Our results indicate that fracture intersection geometries are very complex. Much experimental work with fracture intersection geometries has considered natural fractures to be frictional interfaces that span the entire height of the contained hydraulic fracture. These types of experiments represent a 2D thought process and do not allow for fracture bypass which is likely for subsurface hydraulic fracture / natural fracture intersections. We contend that experimental tests with cemented interfaces that allow for bypass are more realistic to subsurface hydraulic fracture / natural fracture intersections. 2D fracture propagation models (or pseudo-3D models) cannot represent hydraulic fracture bypass or mixed mode I-III propagation. These shortcomings need to be addressed with future modeling work in order to obtain more accurate models.

Non-orthogonal intersections are shown to be more likely to divert fracture propagation, while orthogonal intersections may result in fracture diversion and / or bypassing. Several tests indicate that for oblique hydraulic fracture / natural fracture intersections, the fracture chooses the propagation path along the natural fracture that forms an acute angle ($|\theta| < 90°$) with the in-plane projection of the approaching hydraulic fracture. Although the fracture may continue diverted propagation in only one direction, separation of the weakly bonded interface between the cement and the host rock is likely in both directions. Hydraulic fracture bypass around natural fractures may be a common intersection geometry for cemented fractures where height growth plays an important role. As H_{HF}/H_{NF} decreases, the likelihood of fracture diversion increases. As H_{HF}/H_{NF} increases, the likelihood of fracture bypass increases. The value of H_{HF}/H_{NF} or any other

factor such as cement composition or intersection angle did not seem to have an effect on the likelihood of separation of weakly bonded interfaces. Separation of weakly bonded interfaces was seen in every case of fracture intersection, indicating that weakly bonded interfaces may play an important role in subsurface fracture intersection geometries. One likely fracture intersection geometry is that in which height growth allows the hydraulic fracture to bypass the natural fracture while the fracturing fluid separates the weakly bonded interface between the natural fracture cement and the host rock (filling up the natural fracture if it is permeable).

According to the method outlined by De Pater et. al. (1994a, 1994b), we analyzed the dimensionless groups of time, crack energy, elastic deformation, leakoff, and confining stress. Our analysis indicates that our experiments scale more closely to a typical field high viscosity cross-linked gel fracture stimulation treatment in a tight shale formation. Elastic deformation and confining stress are scaled most closely to the gel scenario field conditions with a lab to field ratio of 0.79 and 0.4 respectively. Given that confining stress has a very strong influence on fracture intersection geometry, it is important that this lab to field ratio be as close to one as possible. Due to operational limitations, the lab to field ratios for time, crack energy, and leakoff were within two orders of magnitude from the desired ratio of one.

The experiments performed represent cases where cemented fractures are similar in strength or stronger than the host rock. For example, these cases are analogous to quartz cement in sandstone (similar strength) or stronger quartz cement in weaker shale. We have not yet performed experiments where the cemented fractures are weaker than the host rock - analogous to a case of calcite cemented natural fractures in shale which are common in the Barnett shale (Gale et. al. 2007). Weaker cemented fractures could

allow the hydraulic fracture to more easily break the cement creating a crossing geometry.

In our experiments, we saw no evidence of crossing even when the cemented fracture was bonded well with the host rock and had the same strength as the host rock, but this was expected due to the low stress state of our experiments. Mathematical analysis of similar experiments with properly scaled confining stress (S_{Hmin} ~ 125psi) indicates that crossing is likely in fracture intersections where the angle of intersection is high. Our crossing analysis suggests that the cement bond strength has a strong effect on crossing. When the cement bond strength is close to the strength of the intact rock, the differential stress has a larger effect on crossing. If the bond strength is lowered to half the strength of the intact plaster, crossing is not likely at any angle.

Theoretically, if the fluid is able to move through the cemented natural fracture without actually breaking it, the approaching hydraulic fracture may still be able to cross by re-initiating growth on the far side through fluid pressure and flaw growth. Our experiments run with natural fractures of different permeabilities ($0 < k_{fracture} < 100$ mD) showed no clear effect that natural fracture permeability had on fracture intersection geometry. However, we did not explore the case in which the natural fractures are essentially open cracks and have extremely high permeability. This might be the case if the natural fracture is partially mineralized.

References

Athavale, A.S., and Miskimins, J.L. 2008. Laboratory hydraulic fracturing tests on small homogeneous and laminated blocks. ARMA 08-067. 42nd US Rock Mechanics Symposium, San Francisco, California, June 29 – July 2.

Beugelsdijk, L.J.L., de Pater, C.J., and Sato,K., 2000. Experimental hydraulic fracture propagation in a multi-fractured medium, SPE 59419, Asia Pacific Conference on Integrated Modeling for Asset Management, Hokohama, Japan.

Blanton, T.L., 1982. An experimental study of interaction between hydraulically induced and pre-existing fractures. SPE/DOE 10847 Unconventional Gas Recovery Symposium, Pittsburgh, Pennsylvania, May 18-21.

Branagan, P.T., Peterson, R.E., Warpinski, N.R., and Wright, T.B., 1996. Characterizatoin of a remotely intersected set of hydraulic fractures: Results of intersection well No. 1-B, GRI/DOE Multi-Site Project. SPE 36452, SPE Annual Technical Conference and Exhibition, Denver, Colorado, October 6-9.

Cooke, M.L., and Pollard, D.D., 1996. Fracture propagation paths under mixed mode loading within rectangular blocks of polymethyl methacrylate. J. Geophys. Res. 101: 3387–3400.

Dahi-Taleghani, A., and Olson, J.E., 2011. Numerical modeling of multistranded-hydraulic-fracture propagation: Accounting for the interaction between induced and natural fractures. SPE Journal (Sept. 2011), 575-581.

Daniels, J., Waters, G., LeCalvez, J., Lassek, J., and Bentley, D., 2007. Contacting more of the Barnett Shale through and integration of real-time microseismic monitoring, petrophysics and hydraulic fracture design. SPE 110562 SPE Annual Conference and Exhibition, Anaheim, California, October 12-14.

De Pater, C.J., Cleary, M.P., Quinn, T.S., Barr, D.T., Johnson, D.E., and Weijers, L. 1994. Experimental verification of dimensional analysis for hydraulic fracturing. SPE Production & Facilities, Nov. 1994, 230-238.

De Pater, C.J., Weijers, Leen, Savic, Milos, Wolf, K.H.A.A., van den Hoek, P.J., Barr, D.T. 1994. Experimental Study of Nonlinear Effects in Hydraulic Fracture Propagation. SPE Production & Facilities, Nov. 1994. p 239-246.

Fisher, N.K., Davidson, B.M., Goodwin, E.O., Buckler, W.S. and Steinberger, N. P., 2002. Integrating fracture mappig technologies to optimize stimulations in the Barnett Shale. SPE 77441 SPE Annual Technical Conference and Exhibition, San Antonio, Texas, Sept. 29-Oct. 2.

Fisher, N.K., Warpinski, N.R., 2012. Hydraulic-Fracture-Height Growth: Real Data. SPE Production & Operations Journal, v. 27, 8-19.

Gale, J. F. W., Reed, R.M., and Holder, J., 2007. Natural fractures in the Barnett shale and their importance for hydraulic fracture treatments. AAPG Bulletin, v. 91, 603-622.

Grieser, B. et al. The Rocket Science Behind Water Frac Design. Paper SPE 80933 presented at the 2003 SPE Production and Operations Symposium, Oklahoma City, Oklahoma, March 23-25.

Gu, H., Weng, X., Lund, J., Mack, M., Ganguly, U. and Suarez-Rivera, R. 2011. Hydraulic fracture crossing natural fracture at non-orthogonal angles: A criterion, its validation and applications. SPE 139984, SPE Hydraulic Fracturing Conference and Exhibition, The Woodlands, Texas, January 24-26.

Jeffery, R.G, Settari, A., and Smith, N.P. 1995. A comparison of hydraulic fracture field experiments, including mineback geometry data with numerical fracture model simulations. SPE 30508, 1995 Annual Technical Conference and Exhibition, Dallas, 22-25.

Laubach, S.E. 2003. Practical approaches to identifying sealed and open fractures. AAPG Bulletin, v. 87, 561-579.

Lawn, Brian R., and T. R. Wilshaw. Fracture of Brittle Solids. Cambridge Eng.: Cambridge UP, 1975. Print.

Le Calvez, J.H., Klem, R., Tanner, K.V., Bennett,L. and, Craven, M., 2007. Real-time microseismic monitoring of hydraulic fracture treatment: a tool to improve completion and reservoir management. SPE 106159 , SPE Hydraulic Fracturing Technology Conference, College Station, Texas, Jan. 29-31.

Lim, I.L., I.W. Johnston, S.K. Choi, and J.N. Boland. 1994. Fracture testing of a soft rock with semi-circular specimens under three point bending, part 1: mode-I. Int. J. Rock Mech. & Min. Sci. & Geomech. Abstr. 31, 3: 185-197.

Maxwell ,S.C., Urbancic, T.I., Steinsberger, N.P., and Zinno, R., 2002. Microseismic imaging of hydraulic fracture complexity in the Barnett shale, SPE 77440 SPE Annual Technical Conference and Exhibition, San Antonio, Texas, Sept. 29-Oct. 2.

Olson, J.E. 2008. Multi-fracture propagation modeling: Applications to hydraulic fracturing in shales and tight gas sands. 42nd Rock Mechanics Symposium and 2nd U.S. – Canada Rock Mechanics Symposium, San Francisco, June 29-July 2.

Park, N., Holder, J., and Olson, J. E., 2004. Discrete Element Modeling of Fracture Toughness Tests in Weakly Cemented Sandstone. Gulf Rocks 2004, the 6th North America Rock Mechanics Symposium, Houston, Texas, June 5 - 9.

Pollard, D.D., and Aydin, A., 1988. Progress in Understanding Jointing Over the Past Century. Geological Society of America Bulletin. 100, no. 8; 1181-1204.

Renshaw, C.E. and Pollard,D.D., 1995. An experimentally verified criterion for propagation across unbounded frictional interfaces in brittle linear elastic materials, Int. J. Rock Mech. & Geomech. Abs., 32 237-241.

Warpinski, N.R. and Teufel. L.W., 1987. Influence of geologic discontinuities on hydraulic fracture propagation. Jour. Pet. Tech., 39 (2), 209-220.

Warpinski, N.R., Lorenz, J.C., Branagan, P.T., Myal, F.R., and Ball, B.L. 1993. Examination of a cored hydraulic fracture in a deep gas well. SPE Production and Facilities (August 1993), 150-158.

Weng, X., Kresse, O., Cohen, C., Wu, R. and Gu, H. 2011. Modeling of Hydraulic Fracture Network Propagation in a Naturally Fractured Formation. Paper SPE 140253 presented at the SPE Hydraulic Fracturing Technology Conference and Exhibition held in The Woodlands, Texas, USA, 24-26 January 2011.

Zhou, J., and Xue, C., 2011. Experimental investigation of fracture interaction between natural fractures and hydraulic fracture in naturally fractured reservoirs. SPE 142890, SPE EUROPEC/EAGE Annual Conference and Exhibition, Vienna, Austin, May 23-26.

Zhou J., Chen,M., Jin,Y., and Ahang,G., 2008. Analysis of fracture propagation behavior and fracture geometry using a tri-axial fracturing system in naturally fractured reservoirs. Int. Jour. Rock Mech. Min. Sci. 45, 1143-1152.

Zoback, Mark. Reservoir Geomechanics. Cambridge University Press, 2007.